



## UvA-DARE (Digital Academic Repository)

### Reducing cross-flow vibrations of underflow gates: experiments and numerical studies

Erdbrink, C.D.; Krzhizhanovskaya, V.V.; Sloot, P.M.A.

**DOI**

[10.1016/j.jfluidstructs.2014.06.010](https://doi.org/10.1016/j.jfluidstructs.2014.06.010)

**Publication date**

2014

**Document Version**

Final published version

**Published in**

Journal of Fluids and Structures

[Link to publication](#)

**Citation for published version (APA):**

Erdbrink, C. D., Krzhizhanovskaya, V. V., & Sloot, P. M. A. (2014). Reducing cross-flow vibrations of underflow gates: experiments and numerical studies. *Journal of Fluids and Structures*, 50, 25-48. <https://doi.org/10.1016/j.jfluidstructs.2014.06.010>

**General rights**

It is not permitted to download or to forward/distribute the text or part of it without the consent of the author(s) and/or copyright holder(s), other than for strictly personal, individual use, unless the work is under an open content license (like Creative Commons).

**Disclaimer/Complaints regulations**

If you believe that digital publication of certain material infringes any of your rights or (privacy) interests, please let the Library know, stating your reasons. In case of a legitimate complaint, the Library will make the material inaccessible and/or remove it from the website. Please Ask the Library: <https://uba.uva.nl/en/contact>, or a letter to: Library of the University of Amsterdam, Secretariat, Singel 425, 1012 WP Amsterdam, The Netherlands. You will be contacted as soon as possible.

*UvA-DARE is a service provided by the library of the University of Amsterdam (<https://dare.uva.nl>)*



ELSEVIER

Contents lists available at ScienceDirect

## Journal of Fluids and Structures

journal homepage: [www.elsevier.com/locate/jfs](http://www.elsevier.com/locate/jfs)

# Reducing cross-flow vibrations of underflow gates: Experiments and numerical studies

C.D. Erdbrink<sup>a,b,c,\*</sup>, V.V. Krzhizhanovskaya<sup>a,c,d</sup>, P.M.A. Sloot<sup>a,c,e</sup><sup>a</sup> University of Amsterdam, The Netherlands<sup>b</sup> Deltares, The Netherlands<sup>c</sup> Saint Petersburg National Research University of Information Technologies, Mechanics and Optics, Russia<sup>d</sup> St. Petersburg State Polytechnic University, Saint Petersburg, Russia<sup>e</sup> Nanyang Technological University, Singapore

## ARTICLE INFO

## Article history:

Received 4 September 2013

Accepted 7 June 2014

Available online 19 July 2014

## Keywords:

Hydraulic gates

Underflow gate

Gate design

Flow-induced vibrations

Physical experiment

Finite Element Method

## ABSTRACT

An experimental study is combined with numerical modelling to investigate new ways to reduce cross-flow vibrations of hydraulic gates with underflow. A rectangular gate section placed in a flume was given freedom to vibrate in the vertical direction. Horizontal slots in the gate bottom enabled leakage flow through the gate to enter the area directly under the gate which is known to play a key role in most excitation mechanisms.

For submerged discharge conditions with small gate openings the vertical dynamic support force was measured in the reduced velocity range  $1.5 < V_r < 10.5$  for a gate with and without ventilation slots. The leakage flow significantly reduced vibrations. This attenuation was most profound in the high stiffness region at  $2 < V_r < 3.5$ .

Two-dimensional numerical simulations were performed with the Finite Element Method to assess local velocities and pressures for both gate types. A moving mesh covering both solid and fluid domain allowed free gate movement and two-way fluid–structure interactions. Modelling assumptions and observed numerical effects are discussed and quantified. The simulated added mass in still water is shown to be close to experimental values. The spring stiffness and mass factor were varied to achieve similar response frequencies at the same dry natural frequencies as in the experiment. Although it was not possible to reproduce the vibrations dominated by impinging leading edge vortices (ILEV) at relatively low  $V_r$ , the simulations at high  $V_r$  showed strong vibrations with movement-induced excitation (MIE). For the latter case, the simulated response reduction of the ventilated gate agrees with the experimental results. The numerical modelling results suggest that the leakage flow diminishes pressure fluctuations close to the trailing edge associated with entrainment from the wake into the recirculation zone directly under the gate that most likely cause the growing oscillations of the ordinary rectangular gate.

© 2014 The Authors. Published by Elsevier Ltd. This is an open access article under the CC BY-NC-ND license (<http://creativecommons.org/licenses/by-nc-nd/3.0/>).

## 1. Introduction

This study presents a novel hydraulic gate design aimed at reducing vibrations induced by underflow. The dynamic response of a hydraulic gate due to its interaction with the flow strongly depends on details of the gate bottom geometry. Numerous

\* Corresponding author.

E-mail address: [chrisedbrink@gmail.com](mailto:chrisedbrink@gmail.com) (C.D. Erdbrink).

experimental studies of flow-induced vibrations (FIV) of gates have previously looked into the characteristics of gate shapes (Hardwick, 1974; Vrijer, 1979; Kolkman, 1984). The gained insight in excitation mechanisms has resulted in widespread rules of thumb for unfavourable designs that should be avoided as well as favourable design features (e.g. Thang, 1990; Naudascher and Rockwell, 1994). However, fundamental knowledge and practical experience have not culminated in one ideal universal shape – partly because the surrounding structure is an important factor. Consequently, hydraulic engineers still stumble on the problem of gate vibrations when designing a new structure or when conditions of gate operation change over time.

Experimental and numerical models are incapable of capturing all degrees of freedom (d.o.f.) experienced by real-life gates (mass-vibration mode in cross-flow and in-flow direction, bending, torsion). Streamwise (horizontal) vibrations are usually studied separately (e.g. Jongeling, 1988) and sometimes in combination with the cross-flow mode (Billeter and Staubli, 2000). In this study we consider the most frequently investigated mode for a vertical-lift underflow gate: one d.o.f. in the cross-flow direction.

The discharge past a partly lifted gate is driven by a head difference, which causes a streamwise pressure gradient. At sufficiently high downstream water levels, the discharge is submerged and a quasi-stationary rotational cell with horizontal axis exists in the downstream region. The flow accelerates as it approaches the gate; the mean velocity reaches a maximum just past the gate in the point of maximal flow contraction called the vena contracta. Depending on the head difference, submergence and the gate's geometry and position, it experiences a steady positive or negative lift force (Naudascher, 1991). This quasi-steady description suffices as long as the gate does not oscillate.

The emergence and severity of flow-related dynamic forces on the gate are related to flow instabilities and body motion effects. To describe and explain relations between flow properties, forces and gate motion during oscillation, several excitation mechanisms were introduced. Periodic fluctuations of the separated flow's shear layer may cause an active response. For gates with a sharp upstream edge, this mechanism is called Impinging Leading Edge Vibrations (ILEV). If the gate bottom has an extending lip in streamwise direction, the shear layer separated from the upstream edge may reattach to the gate bottom in an unstable way, giving dynamic excitation. In a different mechanism, periodic forces are the result of initially small gate movements. This self-exciting process is called movement-induced excitation (MIE). The galloping phenomenon falls in this category.

Previous investigations have proved that most severe vibrations of underflow gates in submerged flow occur at small gate openings and are predominantly caused by ILEV and MIE mechanisms (Hardwick, 1974; Thang and Naudascher, 1986a, 1986b). The current study therefore focuses on small gate openings and does not look at the distinctly different mechanism of noise excitation. Other notable studies are Kapur and Reynolds (1967); Naudascher and Rockwell (1980); Thang (1990); Kanne et al. (1991); Ishii (1992) and Gomes et al. (2011). Overviews of flow-induced vibrations of gates are found in Kolkman (1976); Naudascher and Rockwell (1994) and Jongeling and Erdbrink (2009); Blevins (1990) treats FIV in a wider context. None of these authors considered holes in the gate as a means to weaken vibrations.

Assuming that adding structural damping or avoiding critical gate openings are unfeasible options, the shape of the gate bottom is the decisive factor determining the tendency to vibrate. If the flow passes the gate while remaining attached, or if there is a fixed separation point and a stable reattachment, or if the shear layer is kept away from the bottom in all circumstances, then the ILEV mechanism may be avoided. A thin, sharp-edged geometry with separation from the trailing edge is favourable, since potential shear layer instabilities occur downstream from the gate and a small bottom area inhibits the occurrence of large (suction) forces on the gate, thus minimising the risk of MIE vibrations. But such a design is often not practical or is influenced in an undesirable way by additional details such as flexible rubber seals. The investigation at hand takes the unfavourable thick flat-bottom rectangular gate as a reference gate and introduces a new design with leakage flow through openings in the bottom section as a potential way to improve its vibration properties, see Fig. 1.

Numerical simulations of gate vibrations based on elementary physics equations are inevitably complex and computationally involved. The computational Fluid–Structure Interaction (FSI) model needs to deal with very small displacements of varying

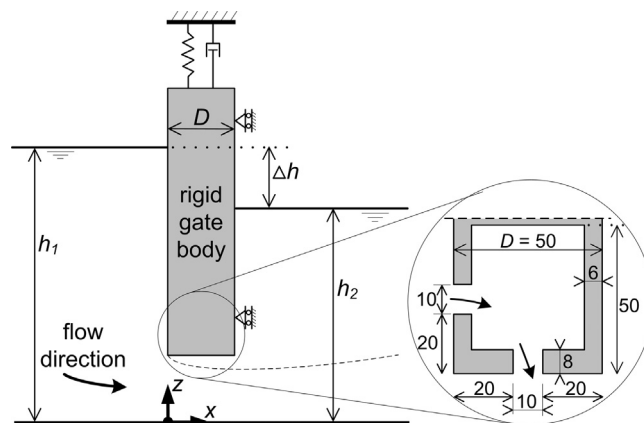


Fig. 1. Streamwise cross-section of gate configuration showing ventilated gate design (detail of bottom element on the right). Dimensions in millimetres, not drawn to scale. Details are given in Figs. 2–4.

frequencies and should represent the boundary forces accurately. The fact that the flow is incompressible, turbulent and has a free-surface adds to the numerical challenge from a Computational Fluid Dynamics (CFD) viewpoint. Many modelling simplifications, such as lowering the fluid's viscosity or including only partial interaction between fluid and solid, are not permitted as they misrepresent the physics too drastically so that excitation mechanisms have no chance to develop correctly. Meshes that do not match up at the fluid–solid interface have the disadvantage of requiring interpolation functions (De Boer, 2008) and dedicated load transfer schemes (Jaiman et al., 2006). Applying the Finite Element Method (FEM) gives the possibility to contain both the solid and fluid domain in one and the same computational moving mesh – thus avoiding a number of coupling issues. Rugonyi and Bathe (2001) explore FEM for FSI problems with incompressible fluid flow.

Numerical studies of gate dynamics are scarce compared to flow-induced vibrations of bluff bodies. The field of Vortex-Induced Vibrations (VIV), see Sarpkaya (2004), tackles a fundamentally different problem and has a much wider range of applications. The flow around stationary and vibrating cylinders has become a classical numerical modelling problem (Al-Jamal and Dalton, 2004; Dai et al., 2013). Numerical modelling of gates often has the goal of verifying the design of a specific hydraulic structure. Determining static support forces is then a greater concern than addressing vibrations (Scheffermann and Stockstill, 2009; Liu et al., 2011). A study on gate control with numerical modelling on different scales, including the influence of the free surface, is provided by Erdbrink et al. (2014). Those studies that do consider vibrations more often than not fail to make links to the existing state of the art, thus not optimally contributing to fundamental knowledge (e.g. Lupuleac et al., 2008).

The two aims of this paper are to provide an investigation into the dynamic behaviour of a perforated gate *and* to assess the feasibility of numerical physics-based modelling as a complementary tool next to physical modelling for evaluating flow-induced vibrations of gates. The motivation behind the second aim is the engineer's desire to develop quick assessment tools for gate designs. Moreover, the growing application of early warning systems to flood defense systems (Erdbrink et al., 2012) calls for numerical models capable of foreseeing risky future situations.

The next section describes the set-up and results of the physical scale model experiment. It includes a paragraph on analysis giving definitions of physical parameters. In Section 3, the numerical model is treated, showing results of validation runs and simulations of a vibration case from the experiment. Section 4 discusses the excitation mechanisms and the working of the gate with slots. The limitations of the numerical model are discussed as well. The final section contains the conclusions and possible future work.

## 2. Physical experiment

### 2.1. Experimental set-up

The experiment of a gate section was performed in a 1 m wide and about 90 m long laboratory flume. A straight, vertically placed underflow gate is suspended in a steel frame that is fixed to the flume. Fig. 2 contains drawings of the placement of the gate and the frame in the flume. The dimensions of the gate are  $1100 \times 600 \times 50 \text{ mm}^3$  (height  $\times$  width  $\times$  thickness); it is a stiff plate and thus acts as a linear mass-spring oscillator body with one degree of freedom in the cross-flow vertical direction. To prevent measurement equipment and frame parts from influencing the flow, the flume was locally narrowed to 0.5 m by constructing side walls out of waterproof film-coated plywood and a sloped ramp of the same material around the gate. In the section closest to the gate, the walls were made out of transparent Perspex plastic to allow visual inspection. The flow directly upstream from the gate was attached to the walls and has low turbulence intensity.

Fig. 3 shows the gate's front view and suspension. As mentioned in the Introduction, two gate types were tested. The flat rectangular-shaped bottom (with smooth surface, sharp edges and without extending lip) will be called 'original gate'. The adapted gate differs from the original gate in that it has five horizontal slots in the upstream face of the bottom section, as shown in Fig. 3, and five identical slots in the bottom face of the bottom section, as shown in Fig. 4. This gate will be called 'ventilated gate'. The slots on the upstream side act as inflow openings for leakage flow and the slots on the downward facing side act as outflow openings. The dimensions of the slots were chosen such that the effect of the leakage would be distinctly perceptible, but without compromising the rigidity of the gate.

The gate is supported in vertical direction by three springs, one spring in the centre with adjustable stiffness and two side springs of lower stiffness. Prior to each measurement, the gate was set to the desired height and the main central spring was set to the desired stiffness. Then the tension in the two side springs was adjusted (symmetrically) by changing the length of the chains connecting the side springs with the frame, see Fig. 3. This was done in such a way that the two low stiffness side springs carried most of the static loads in vertical direction. The dynamic loads were mostly carried by the stiff central spring. Its adjustable stiffness enabled a controlled variation of the natural frequency. For the two weak side springs, linear coil springs (Alcomex TR-1540) were used; for the stiff main spring a double leaf spring was custom-built with high yield strength steel and a high elastic limit (Armco 17-7PH, hardening condition TH1050).

The two bending blades of the main spring have dimensions  $600 \text{ mm} \times 30 \text{ mm} \times 4 \text{ mm}$  ( $l \times b \times t$ ). The bending length  $L$  ( $< 600 \text{ mm}$ ) can be adjusted by movable blocks with clamps, thus varying structural stiffness, see Fig. 3. Linearity of this spring was confirmed by static loading tests for different bending lengths. The main spring is installed in parallel with two side springs, each with constant  $k_{\text{side}} = 0.57 \text{ N/mm}$ . The relation between bending length and total stiffness of the three

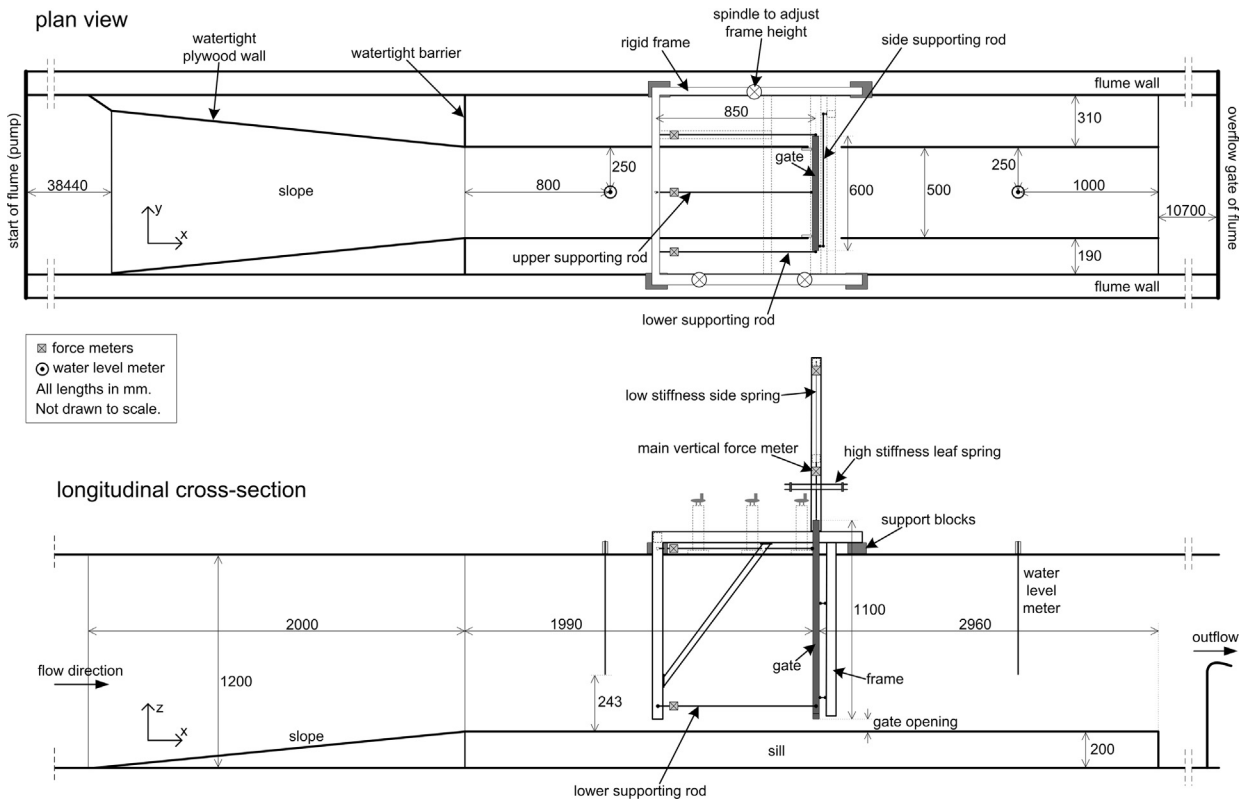


Fig. 2. Set-up of gate experiment in the flume.

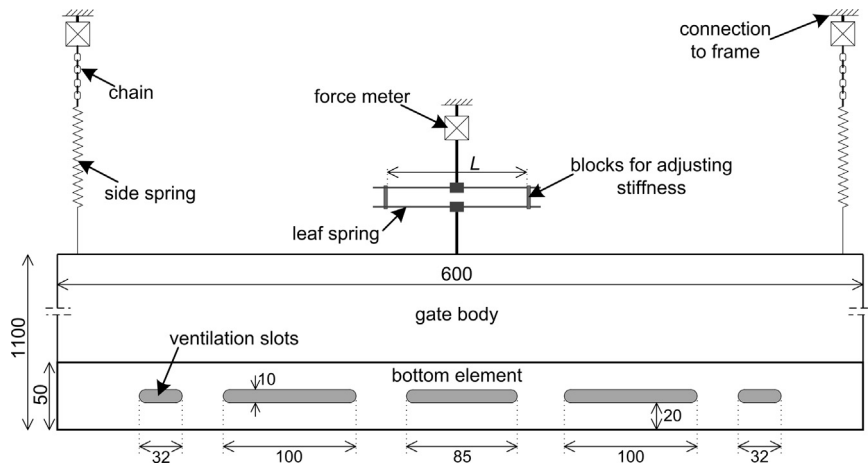


Fig. 3. Front view from upstream side showing inflow ventilation slots in the bottom section of the gate and the three supporting springs. Measurement frame is left out for clarity. Measurements are in millimetres. Only the bottom element is drawn to scale.

springs is derived from constitutive relations plus Hookes law

$$k_{total} = k_{main} + 2k_{side} = \frac{8Ebt^3}{L^3} + 1.14, \tag{1}$$

where  $k_{total}$  is the combined spring stiffness in N/mm,  $E$  the modulus of elasticity in N/mm<sup>2</sup>,  $b$  the width and  $t$  the thickness of the leaf spring blades in mm and  $L$  the length between the clamps in mm. This formula was calibrated with free vibration tests in air to increase accuracy between chosen  $L$  and achieved  $k_{total}$  and dry natural frequency  $f_0$ .

The main gate body consists of a rigid steel grid filled with water-resisting foam and covered with thin plastic plates on both sides. The bottom element is carved out of PVC material and is screwed onto the main body, thus forming one stiff mass with it. In order to reduce weight, the bottom element is hollow; it contains five chambers (see Fig. 4). The total mass of the

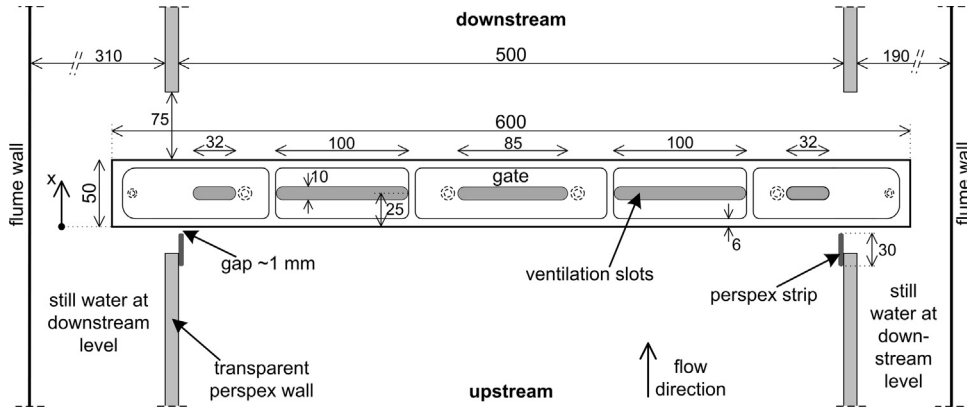


**Fig. 4.** Plan view of gate with cross section through bottom element revealing the outflow slots in the bottom face of the gate. The supporting frame is left out for clarity. Measurements in millimetres. Only the gate is drawn to scale.

original gate was 17.2 kg. The bottom element of the ventilated gate is lighter due to removal of material, but the openings allow more water into the cavities of the bottom element so that the total mass of the modified gate was only slightly higher: 17.3 kg. These values exclude added mass due to water displacement during oscillation.

A plan view of the gate is sketched in Fig. 4. The water flows between the perspex walls, in the figure from bottom to top. The space between the perspex walls and the flume walls is filled with still water at the downstream water level. The side seals consist of thin vertical strips that are carefully installed such that side leakage is minimised and at the same time no contact is made with the gate. Observations during the experiment indicated that the inevitable sideways leakage was only significant at relatively high hydraulic heads, although the leakage appeared to be only a small fraction of the total gate discharge. It was also observed that the distance between gate and side walls on the downstream side had little impact on the underflow discharge. Fig. 4 contains a gate cross-section through the bottom section, such that the outflow openings of the ventilated gate become visible. These five openings are identical to the five openings on the upstream face of the gate. All slots were cut perpendicularly to the faces, see Fig. 1.

Five horizontal supports, three hinged steel rods in longitudinal direction and two in cross direction, enable vertical movement of the gate while fixing the gate position horizontally. Six force metres were installed: vertically one for each spring and horizontally one for each longitudinal support. Only the main vertical support force is used in the analysis of the gate response. The sample frequency was 200 Hz. The length of the analysed data files was 90 s on average and had a minimum of 60 s, yielding a frequency resolution of at least 0.0017 Hz. Recording started after reaching equilibrium water levels and horizontal support forces. The signal analysis done in MATLAB consisted of standard FFT-analysis using sliding windows. Furthermore, the discharge and the water levels on the upstream ( $h_1$ ) and the downstream side ( $h_2$ ) of the gate were measured using resistance-type water level metres. The locations of the water level metres are shown in Fig. 2. See Erdbrink (2012) for more details on the experimental set-up.

## 2.2. Analysis and definitions

The motion equation in vertical  $z$ -direction for partly submerged bodies has to include hydrodynamic or ‘added’ coefficients (see e.g. Kolkman, 1980)

$$(m + m_w)\ddot{z} + (c + c_w)\dot{z} + (k + k_w)z = F(t, z, \dot{z}), \quad (2)$$

here,  $m$  is the mass,  $c$  is the damping,  $k$  is the stiffness,  $F$  is the excitation force and the subscript  $w$  indicates the added coefficients. The dependency of  $F$  on displacement and velocity represent non-linear coupling. For the same body vibrating in air, we have (Den Hartog, 1956)

$$\ddot{z} + 2\zeta\omega_0\dot{z} + \omega_0^2z = F/m, \quad (3)$$

using the damping ratio  $\zeta$  and the undamped natural angular frequency in air  $\omega_0 = \sqrt{k/m} = 2\pi f_0$ . For the damped case,  $\omega_0$  and  $f_0$  have to be multiplied by a factor  $\sqrt{1 - \zeta^2}$ . The excitation is a time-dependent hydraulic force which can be written as

$$F = \frac{1}{2}C_F\rho U^2 WD = C_F F_0, \quad (4)$$

where  $W$  is the cross-flow width of the gate section on which  $F$  works,  $F_0$  is a stationary reference fluid force and  $C_F$  is a force coefficient equal to

$$C_F = C'_F \sin(\omega t + \varphi), \quad (5)$$

where  $\varphi$  is the phase shift between excitation and displacement. Note that in this study not the displacement  $z$  but the response force  $F_z$  is measured, the amplitude of which is denoted  $\hat{F}_z$ . Furthermore, for the pressure on the gate bottom boundary  $p_{\text{bound}}$  we

use the pressure coefficient  $C_p$  defined logically as  $p_{\text{bound}}$  divided by  $\rho g \Delta h$ . The two-dimensional discharge formula for an underflow gate section in submerged flow is

$$q = C_D a U = C_D a \sqrt{2g\Delta h}, \quad (6)$$

with  $q$  the discharge per unit width in  $\text{m}^3/\text{s}/\text{m}$  or  $\text{m}^2/\text{s}$ ,  $C_D$  the dimensionless discharge coefficient for submerged flow,  $a$  the lifting height or gate opening,  $U$  the flow velocity in the vena contracta, estimated with Bernoulli's formula, in  $\text{m}/\text{s}$  and  $\Delta h = h_1 - h_2$ . The reduced velocity  $V_r$  is used as dimensionless descriptive quantity for the flow-induced vibrations. It is defined here as

$$V_r = \frac{\sqrt{2g\Delta h}}{f_z D}, \quad (7)$$

where  $f_z$  is the dominant response frequency, the numerator represents the characteristic flow velocity and the gate thickness in flow direction  $D$  (see Fig. 1) is taken as characteristic length scale. In the present study, the added mass  $m_w$  is estimated experimentally in still water by free vibration tests in air and still water. It follows from:

$$\frac{f_{0,\text{water}}}{f_0} = \sqrt{\frac{1 + k_w/k}{1 + m_w/m}}, \quad (8)$$

because the added rigidity (hydraulic stiffness)  $k_w$  due to buoyancy on the submerged part of the gate is found via Hooke's law:  $k_{w,\text{buoyancy}} = \rho g W D$ . The error made by neglecting damping here is less than 2%. Numerically,  $m_w$  near a wall in still water was computed in a potential flow model with a finite difference method by Kolkman (1988), and studied many times since then in the context of gates (e.g. Anami et al., 2012). A very universal approach is the observation in Kolkman (1984) that the total kinetic energy of the fluid can be expressed as

$$E_{\text{kin}} = \frac{1}{2} m_w \dot{z}^2. \quad (9)$$

Summing the velocity magnitude over all computational nodes should yield a value for  $m_w$ , assuming that the object velocity is known.

### 2.3. Measurement conditions and variation of parameters

The measurement procedure was to vary  $V_r$  and  $a/D$ , which was done mostly by changing suspension stiffness and gate height and occasionally by changing the pump discharge and height of the outflow weir of the flume. The present study deals with the critical gate opening range for cross-flow vibrations: 98% of the measurements lie in the interval  $0.48 \leq a/D \leq 1.50$ . During the experiment the stiffness was varied between and 19.3 N/mm and 967 N/mm, corresponding to a range in achieved undamped natural frequency in air of  $5.33 \text{ Hz} < f_0 < 37.7 \text{ Hz}$  for the original gate with closed bottom section. The gate submergence  $C_s = (h_2 - a)/D$ , with  $h_2$  the water depth measured downstream from the gate was in the range  $4.2 < C_s < 6.2$ , for 98% of the data. This means flow conditions were close to fully submerged with minor free surface fluctuations. Discharge coefficient  $C_D$  is estimated from the measured pump discharge to be on average 0.80 with standard deviation 0.11 for the original gate and on average 0.83 with standard deviation 0.10 for the ventilated gate. The achieved  $V_r$  ranges were  $1.2 < V_r < 11.6$  for the original gate and  $1.8 < V_r < 9.5$  for the modified gate. The Reynolds number defined as  $\text{Re} = UD/\nu$ , again with  $U = (2g\Delta h)^{0.5}$ , was in the range  $3.2 \times 10^4 < \text{Re} < 1.3 \times 10^5$ . The mass ratio, defined as  $m_r = (m + m_w)/(\rho D^2 W)$ , is computed for the original gate as  $12.3 \leq m_r \leq 12.7$ , and for the ventilated gate as  $12.3 \leq m_r \leq 12.8$ .

Damping was monitored throughout the experiment in 32 free vibration tests in still water, where the gate was set in motion by a manual tap on the top. For each test, the logarithmic decrement of damping  $\delta$  was determined over the first ten periods. At small damping levels, we have  $\delta \approx 2\pi\zeta$ . This formula is used to compute values of the damping ratio  $\zeta$ . For the original gate,  $\zeta$  was on average 0.013 and had a standard deviation of 0.0065. For the ventilated gate, the average value of  $\zeta$  was 0.020 with a standard deviation of 0.0061. The damping values contain no trends related to water depth or stiffness and did not change over time during the experiment. However, there is some inherent variability caused by the manual excitation force not being the same each time. Also, it makes a difference which part of the decaying free vibration is used for determining  $\delta$ . The ventilated gate showed a small number of deviant values of higher damping at small openings  $a/D < 0.7$ , these are not included in the given ranges. The highest recorded damping ratio in this particular situation was  $\zeta = 0.093$ . A possible explanation is that flow resistance inside the chambers between the inflow and outflow slots is more pronounced at small gate openings due to higher relative velocities. Furthermore, even though damping was not higher at larger water depths in still water, the observed leakage through the side seals at high hydraulic heads (that existed for a small part of the measurements) may have had a significant effect on damping due to skinplate friction. This was not quantifiable, since the free vibration tests were only feasible in stagnant water.

The dimensionless Scruton number combines the mass and damping ratios and is, for low damping, defined by  $\text{Sc} = 2m_r\delta = 4\pi m_r\zeta$ . It was found that for the original gate  $1.0 \leq \text{Sc} \leq 2.3$  and for the ventilated gate  $0.9 \leq \text{Sc} \leq 3.7$ . The variation in the Scruton number is almost completely due to the discussed variation in damping. The outliers for the ventilated gate at small openings are not included in the  $\text{Sc}$  ranges. Table 1 gives additional information on measurement conditions.

**Table 1**  
Flume settings during measurements.

	Min	Max	Unit
Pump discharge, $Q_{\text{pump}}$	13.0	50.0	l/s
Gate opening, $a$	22.5	100	mm
Upstream water depth, $h_1$	0.297	0.656	m
Downstream water depth, $h_2$	0.120	0.352	m
Head difference, $\Delta h$	0.063	0.355	m

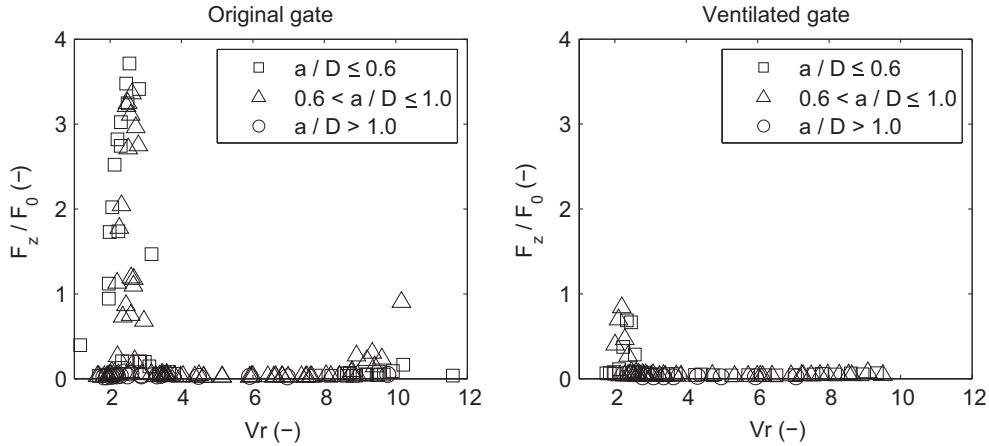


**Fig. 5.** Overview of vibration characteristics of the original rectangular gate (left) and the new ventilated gate (right): reduced velocity  $V_r$  versus dimensionless vibration amplitude  $\hat{F}_z/F_0$  of the main vertical force metre;  $a$  is the gate opening, gate thickness  $D$  is 50 mm.

Parameter ranges given in Table 1 are based on the combined data set for both gates, consisting of 145 measurements for the original gate plus 85 measurements for the modified gate. The achieved underflow discharge was somewhat lower than the pump discharge as a result of the sideways leakage through the seals. An observed variation in the pump discharge of  $\pm 0.5$  l/s was of little influence since the frequency of this variation was very small compared to signal recording length.

#### 2.4. Results of physical experiment

The focus of the experimental data analysis is on determining how dominant force amplitudes in cross-flow direction change with  $V_r$  for both gate types. Absolute maximum force amplitudes depend on structural damping of a particular set-up and are of less interest; therefore response amplitudes are presented for different settings relative to the stationary hydrodynamic force  $F_0$ .

Fig. 5 shows the dimensionless dynamic force response of the closed gate and the ventilated gate. Judging from the plot, the response may be divided into three different regions:  $2 < V_r < 3$  (relatively high stiffness),  $3 < V_r < 8.5$  (medium stiffness) and  $V_r > 8.5$  (relatively low stiffness). Response values of  $\hat{F}_z > 5N$  represent significant, regular oscillations with response frequencies in the range  $4.6 \text{ Hz} < f_{\text{resp},z} < 20.2 \text{ Hz}$ . Vertical displacement amplitudes estimated from the force amplitude as  $\hat{z} = \hat{F}_z/k$  were overall less than  $0.1D$ . The strongest recorded force amplitude in the high stiffness region was found at  $V_r = 2.54$ . The maximum response in the relatively low stiffness vibration region occurred at  $V_r = 10.16$ . The excitation mechanisms associated with these two regions are discussed in Section 4.1.

The results show that the vibrations found at low  $V_r$  occur quite suddenly. There are steep increases in force amplitude around  $V_r = 2$  and  $V_r = 3.0\text{--}3.5$ ; most significantly for gate openings less than or equal to  $D$ . Tests at gate openings smaller than  $0.5D$  were hindered by the risk of the gate hitting the flume bottom. Although the gate opening was not varied over a large range, the data seems to show that the force response at  $V_r \approx 2.5$  occurs at a smaller gate opening than for the response maximum at  $V_r \approx 10$ . Zooming in on the densely sampled area of relatively high frequency response at  $2 < V_r < 3$  gives further insights (Fig. 6). The measurements were done by making series of about ten data points of different stiffness settings, keeping gate opening and discharge constant.

These results reconfirm that in this reduced velocity region significant cross-flow vibrations occur at gate openings in the range  $0.5D \leq a \leq D$ . For  $1.5 < V_r < 4$ , with the strongest force amplitudes around  $a/D = 0.5$ . From Fig. 6 it appears that for head differences  $\Delta h \approx 1.5D\text{--}1.75D$ , vibration maxima decrease with increasing gate opening. The series with high head difference  $\Delta h = 283 \text{ mm} \approx 5.7D$  differs from the rest by its higher hydraulic head and higher stiffness settings. Because the still water damping tests proved that damping is not significantly higher for high spring stiffness settings, the most likely explanation

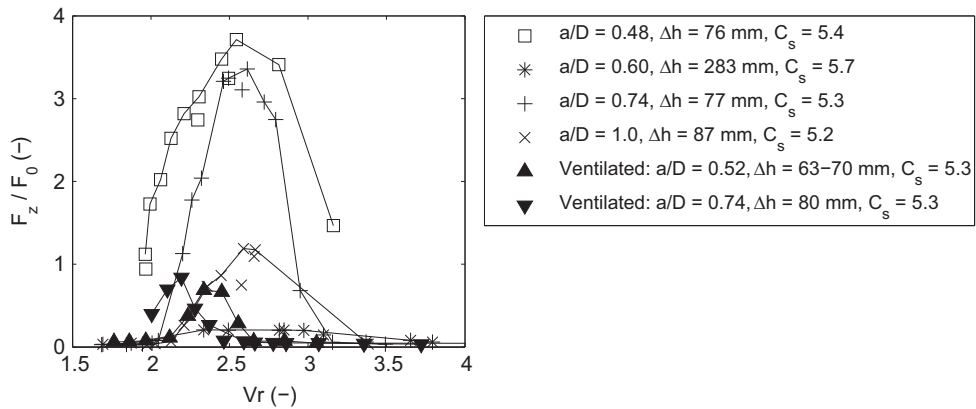


**Fig. 6.** The most significant vibrations at  $1.5 < V_r < 4$ . Measurements series represent constant gate opening  $a/D$  and head difference  $\Delta h$  for varying suspension stiffness. Gate submergence relative to downstream level is denoted  $C_s$ . The solid triangles mark the gate with slots, all other symbols denote the original gate. Responses with  $F_z/F_0 < 0.25$  not belonging to these series are left out for clarity.

of the smaller response of this series is an increased damping associated with the higher hydraulic head. This is possibly related to the observed leakage through the side seals at high hydraulic head. This finding does not influence the comparisons between the two gate types. However, the reported higher damping for the ventilated gate at  $a/D < 0.7$ , see Section 2.3, suggests that the responses of the ventilated gate series at  $a/D = 0.52$  are underestimated.

Despite the smaller data set size of the new gate design, the overall effect of applying ventilation holes seems clear. For very similar conditions at  $1.5 < V_r < 3.5$ , the force amplitude of the vibration is a factor 3 less for the rectangular gate with added holes. For  $3.5 < V_r < 9.5$ , the holed gate shows a very low response for similar conditions (openings and head difference) as the original gate. From the available data points at  $V_r > 8.5$ , the picture of the effect of adding holes is incomplete. More data is needed for  $V_r \geq 10$ . The available data suggests that the ventilation succeeds in having a mitigating effect on the vibrations in that range as well.

The ventilated gate shows an overall shift towards lower achieved  $V_r$  values compared to the original gate. The maximum force response of the new gate lies at  $V_r = 2.19$ . Also, this maximum is found at a higher gate opening than the maximum of the closed gate (0.74D against 0.48D). This is the net effect of the altered gate design: a slightly different mass and additional discharge caused by the jet of relatively high velocity through the gate.

## 2.5. Comparison with other experimental results

The measurement data of the original rectangular gate resembles results from previous experimental research. It is important to realise that most other studies measure response in displacement instead of force. In the high stiffness at  $V_r < 5$ , which has been studied most frequently, the reduced velocity at which highest amplitude is found lies close to  $V_r = 2.75$  found by Hardwick (1974) and  $V_{r,nat} = 2.5$  found by Thang and Naudascher (1986a, 1986b). The reduced velocity based on the natural frequency  $V_{r,nat}$  is somewhat lower than the  $V_r$  used in this study. The gate openings of maximum amplitude were  $a/D = 0.67$  and  $a/D = 0.65$  for these two studies, slightly higher than what is found here. Billeter and Staubli (2000) report maximum force coefficients in z-direction at  $V_r = 2.75$  and  $V_r = 3.0$ .

The experiments of Vrijer (1979) covered vibrations in the range  $10 < V_r < 80$ . Their model dimensions were smaller (gate width of 10 mm). A comparison based on the small overlap of less than ten data points suggests that the lower bound of vibrations in the low stiffness region in the present study is at a slightly lower  $V_r$  value ( $V_r = 9.0$ – $9.5$ ) than in Vrijer (1979) where amplitudes start to increase for  $V_r > 10$ .

## 3. Numerical simulations

### 3.1. Model description

The goal of the numerical simulations is to describe the physical features that are decisive for causing the difference in response between the two gate types. The numerical model is two-dimensional in the vertical direction (2DV) and has a two-way coupling between fluid and solid. Model dimensions are identical to the physical scale model. The flow-wise model length is 3.5 m. The static vertical equilibrium is achieved by a suspension support force equal to the difference between gravitational and buoyancy and mean lift forces. The flow velocity vector is defined as  $\mathbf{u} = (u, v)$ , the displacement vector of the solid body is written  $\mathbf{u}_s$ . The fluid flow is modelled by the incompressible Reynolds-Averaged Navier–Stokes (RANS) equations in combination with the standard  $k$ – $\epsilon$  turbulence model. The solid domain includes deformation due to stresses.

**Table 2**  
Selected cases for numerical simulations (values from experiment).

	Q (l/s)	k (N/m)	$h_1$ (m)	$\Delta h$ (m)	$a/D$ (dimensionless)	$V_r$ (dimensionless)	Cs (dimensionless)	$f_z$ (Hz)	$\hat{F}_z$ (N)
<b>Case 1</b>	23	82502	0.398	0.088	1.00	2.6	5.2	10.1	25.6
<b>Case 2</b>	40	19298	0.605	0.285	0.86	10.2	5.5	4.66	63.0

The governing equations are

$$\rho \frac{\partial \bar{\mathbf{u}}}{\partial t} + \rho \bar{\mathbf{u}} \cdot \nabla \bar{\mathbf{u}} + \nabla \cdot \overline{(\rho \mathbf{u}' \otimes \mathbf{u}')} = -\nabla \bar{p} + \nabla \cdot \mu (\nabla \bar{\mathbf{u}} + (\nabla \bar{\mathbf{u}})^T) + \mathbf{F}_g \text{ and } \nabla \cdot \bar{\mathbf{u}} = 0 \text{ (fluid),} \quad (10)$$

$$\rho_s \frac{\partial^2 \mathbf{u}_s}{\partial t^2} - \nabla \cdot \boldsymbol{\sigma}_s = \mathbf{F}_v \text{ (solid),} \quad (11)$$

where  $\rho$  is the density of water,  $p$  the water pressure,  $\mu$  is the viscosity of water,  $\mathbf{F}_g$  the gravitational force and using Reynolds decomposition  $\mathbf{u} = \bar{\mathbf{u}} + \mathbf{u}'$ . Furthermore,  $\rho_s$  is the solid's density,  $\boldsymbol{\sigma}_s$  are the body stresses and  $\mathbf{F}_v$  are the external forces on the body consisting of gravity, spring force, suspension force and the hydrodynamic forces. The upstream flow boundary condition is a block velocity profile and the downstream boundary is a hydrostatic pressure profile. The transient runs are preceded by stationary pre-runs with the gate held fixed in order to iteratively determine the inlet velocity at which the upstream pressure away from the gate is zero at the surface. [Appendix A](#) gives more details.

The Finite Element Method (FEM) is applied for spatial discretisation. The Arbitrary Lagrangian-Eulerian (ALE) method is used to make a moving mesh for the entire model domain (see e.g. [Ferziger and Perić, 2002](#)). This means the grid adapts to the motion of the oscillating body without changing its connectivity. The free surface boundary is modelled as a rigid lid, which slightly bends up and down with the grid. A set of hyperelastic equations is solved to smooth the displacements of interior cells. The grid consists of unstructured triangular elements and inflated boundary refinements adjacent to the gate walls and flow bottom. A typical grid contained around 35 000 elements and 200 000 degrees of freedom. The cell size in the near-wall flow regions is dictated by the dimensionless wall distance by ensuring that  $y_{\max}^+ = 11.06$  at all walls where wall functions are applied (see [Appendix A](#) and [COMSOL, 2013](#)). The online material contains a movie of the ALE moving mesh.

The FEM solver COMSOL Multiphysics v4.3a ([COMSOL, 2013](#)) is used to solve the system of equations of seven dependent variables. The solution procedure is solved in a fully coupled way with the PARDISO direct solver. The implicit Backward Differentiation Formula (BDF) with adaptive time stepping is used, an extension of the backward Euler method for variable order. The simulations were done on a cluster, using 24 cores on a single node. Typically, three seconds of simulated time took around 12 h of computing time.

Two cases from the experimental data set are selected for simulation; these are representative of strong vibrations in the low and high  $V_r$  region. See [Table 2](#).

### 3.2. Model validation results

We are interested in the behaviour of both gates for conditions as close as possible to those found in the experiment. The followed approach was to assign applicable physical parameters from the experiment to the numerical model. Firstly, the added mass coefficient  $m_w$  in still water is derived from a zero discharge model and compared to experimental values. Secondly, iterative validation runs are made in a model *with* discharge to achieve the settings necessary for attaining the response frequency as found in the experiment. These two preparatory modelling steps should be seen as efforts towards model validation (comparing the modelled value of a universal physical parameter with the experimental value) and calibration (adjusting the numerical model for the specific modelling task), respectively.

#### 3.2.1. Added mass validation

The kinetic energy approach is followed to find  $m_w$  in still water (see [Section 2.2](#)). Because flow velocities are low, the laminar incompressible flow equations are solved. The oscillating gate is simulated by a moving wall with a prescribed vertical periodic velocity with a frequency of 4.7 Hz and amplitude of 0.15 m/s. The rigid lid assumption is justified for this situation because the wave radiation effect is small: for  $h=0.40$  m, we have  $\omega^2 h/g = 36 \gg 10$ , the usual criterion for wave radiation ([Kolkman, 1976](#)).

In [Fig. 7](#) experimental values of non-dimensional added mass in still water are plotted for three water depths, together with simulation results for  $h=0.40$  m. The added mass simulations show that the wall proximity effect at low  $a/D$  is somewhat more pronounced than in the available experimental values. For vibrations at high gate openings, the influence of the bottom disappears. The simulations show a gradient reduction in correspondence with this, while experimental data at higher  $a/D$  would be needed to cover this stabilisation. The experimental data by [Nguyen \(1982\)](#) in [Naudascher and Rockwell \(1994\)](#) show stabilisation of the added mass for  $a/D > 2-3$ . The dependence on water depth that is shown by the experimental values is not sufficiently captured by the FEM model: for other water depths, the results are too close to the

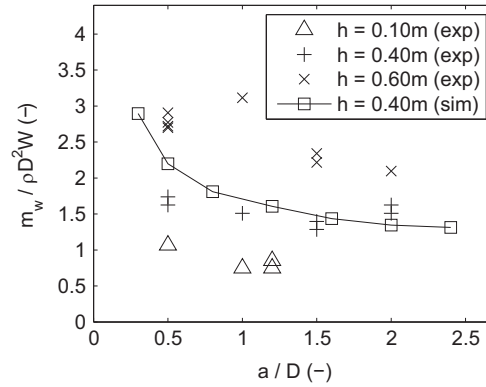


Fig. 7. Added mass coefficient in still water for various openings  $a$  and water depths  $h$ , from experiment (exp) and simulations (sim).

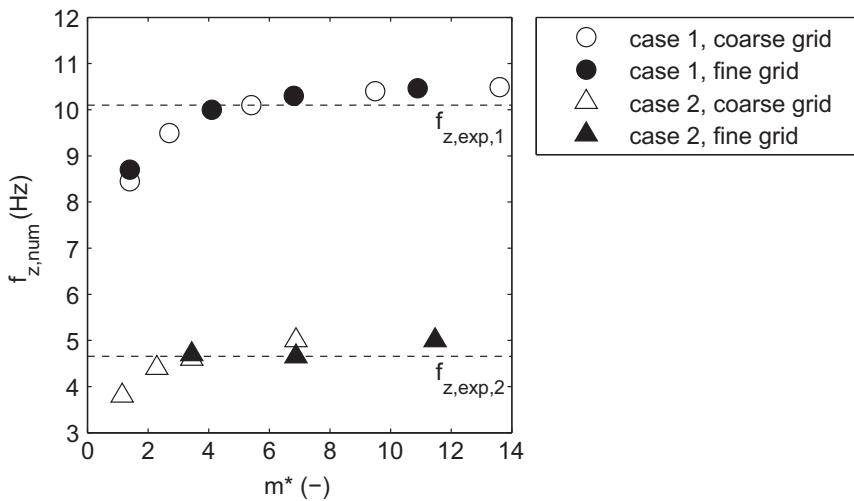


Fig. 8. The artificial added mass effect for the two cases of Table 2. The simulated frequencies  $f_{z,num}$  are given for different mass factors  $m^*$ . For both cases, all data points have the same theoretical natural frequency. The horizontal lines show the experimental response frequencies  $f_{z,exp}$ .

plotted relation for  $h=0.40$  m. The influence of domain width was neutralised by ignoring very small flow velocities in the computation. In summary, for the flow cases that are considered in this study the physical added mass is reasonably well approximated.

### 3.2.2. Artificial added coefficients

In the numerical model, the gate mass is defined by assigning a solid density  $\rho_s$ , and the suspension stiffness  $k$  is defined in a spring suspension support. The added rigidity  $k_w$  due to buoyancy is in all studied cases negligibly small, i.e.  $k_w \ll k$ . Despite the fact that for oscillating bodies in flowing water  $m_w$  and  $k_w$  are in general not equal to their still water values (nor constants for that matter), it is reasoned that mismatches of simulated response frequencies with experimental values, must be traced back to artificial added coefficients. Such misrepresentations were indeed found. It was checked that the natural frequency of the isolated gate in vacuum calculated by the same FEM model exactly matched the analytical value.

A possible cause of numerical complications in FSI is the so-called ‘artificial added mass’ effect. This has been investigated and partially described and explained for sequentially staggered schemes (Förster et al., 2007), but no literature was found for FSI with fully coupled schemes in FEM for relatively stiff solids. Similar to Jamal and Dalton (2004), we define the mass factor  $m^*$  to be the ratio of solid density over fluid density. The term ‘mass ratio’ is also used for this sometimes but can be confused with the dimensionless mass  $m_r$ . The sensitivity of the simulated response frequency  $f_{z,num}$  to the mass factor  $m^*$  is plotted in Fig. 8.

Using the true mass factor of the experiment, which is less than one, gives crude underestimates of the measured response frequency  $f_{z,exp}$  for both investigated cases. The mass factor is increased to  $m^*=1.1$  simply by using a lower gate height in the simulation than in the experiment. When  $m^*$  is increased further by means of increasing solid density  $\rho_s$ , while at the same time adjusting  $k$  proportionally such that the dry natural frequency  $f_0$  remained constant, the numerical model gives better estimates of  $f_{z,exp}$ . Grid refinements did not noticeably influence the trends.

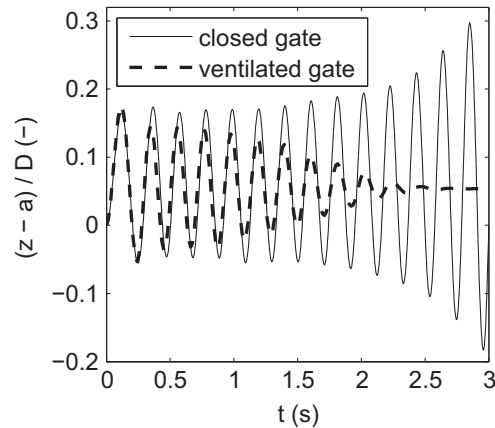


**Fig. 9.** Simulated vertical displacements of original, closed gate (thin continuous line) and gate with ventilation slots added (thick dashed line). The displacement is plotted relative to the original gate position  $z=a$  and normalised to the gate width  $D$ .

Increasing  $m^*$  at fixed  $f_0$  does not yield an asymptotic approach to the experimental values, however. In addition, the achieved displacement amplitudes of the gate vibration are inconveniently small for  $m^* \geq 10$  (order 0.1 mm and smaller). As a tradeoff it is decided to take  $m^*=3$  and adapt  $k$  accordingly so that natural frequency and response frequency are well represented by the numerical model for both cases and displacements are in order of millimetres. It is noted that this measure distorts the absolute values of the modelled displacements.

### 3.3. Results of calibrated numerical model

Next, cases 1 and 2 were simulated with the calibrated numerical model. In each transient run, only three to four seconds were simulated. The numerical perturbations related to initialisation of the run were enough to kick-start a vibration – then the simulated vibration either quickly grew in amplitude or damped out. After a substantial number of test runs, no active response has been found for cases 1 for neither gate type. This is presumably related to an underestimation of the dynamics of the impinging shear layer, see Section 4.1. For case 2 growing amplitudes were found at a slightly larger gate opening than in the experiment (46 mm in the simulation versus 43 mm in the experiment). All plots in this section are simulations of case 2; subsequent analysis also focuses on case 2. Movies of simulation case 2 in the online material show velocity and turbulent kinetic energy fields for both gates.

Fig. 9 shows time signals of the simulated displacement normalised to the gate width  $D$ . After an initially similar disturbance, the ventilated gate follows a damped vibration and the original gate is amplified. The frequency of the ventilated gate is a little lower than the closed gate.

Appendix B provides a closer look on the displacement signal, giving also acceleration and lift force oscillation, see Fig. B1. A number of plots is made in Figs. 11–17 for further comparison of the modelled response of both gate types. Fig. 10 gives the locations of output profiles for pressure, velocity and turbulent kinetic energy, which are plotted in Figs. 11–15.

In each plot of Figs. 11–15, the nine thin lines correspond to different moments in one full sine period, according to  $i\pi/4$  with  $0 \leq i \leq 8$ , starting in equilibrium position (moving upwards) at  $t=1.35$  s. For the original gate, the  $i$  values are indicated explicitly. Additionally, Figs. 11–15 display the situation where the gate is fixed at the equilibrium position for both gate types. The variation of flow parameters is much smaller in the fixed gate scenario and therefore these are depicted as single thick dashed lines, which denote time-averaged values over two consecutive periods, after four seconds of simulation. Figs. 11–15 show that the oscillating ventilated gate experiences significantly lower periodic variation in streamwise pressure, velocity and turbulent kinetic energy (TKE) at the trailing edge, and in bottom pressure, than the gate without holes. Obviously this is associated with the difference in displacement amplitude at the time of output, but nevertheless an insightful comparison can be made.

The streamwise pressure plot (Fig. 11) shows that, at a height of half the gate opening, the original gate experiences larger temporal variation and higher maximum streamwise pressure gradients directly under the gate ( $0 < x/D < 1$ ) than the ventilated gate. The latter experiences low  $dp/dx$ -values for  $x/D < 2$ . The  $u$ -velocity profiles (Fig. 12) clearly show the influence of the extra stream through the hole. For the ventilated gate the area of negative streamwise velocity is very limited,  $0.8 < z/a < 1$  versus  $0.7 < z/a < 1$  for the original gate, and the negative  $u$ -velocities are much smaller as well.

The effect of the downward jet through the hole on  $v$ -velocity (Fig. 13) is that the outflow direction through the slot is now almost completely downward during the whole oscillation period, whereas significant upward velocities exist for the original gate. The TKE plots in Fig. 14 show that the TKE maximum is greatly reduced. In the ventilated case, there are no large TKE levels close to the gate and maximum levels occur around  $z=0.75a$ . The asymmetric shape of the TKE profile of the ventilated gate is due to the combined presence of two shear layers, resulting from flow separation from the

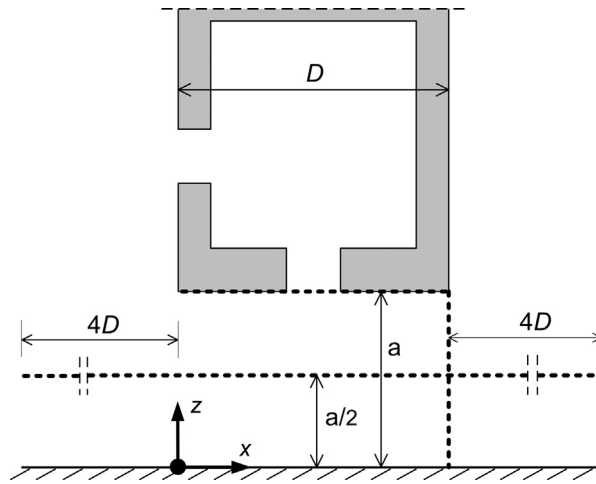


Fig. 10. Location of output profiles (dashed lines) used in Figs. 11–15.

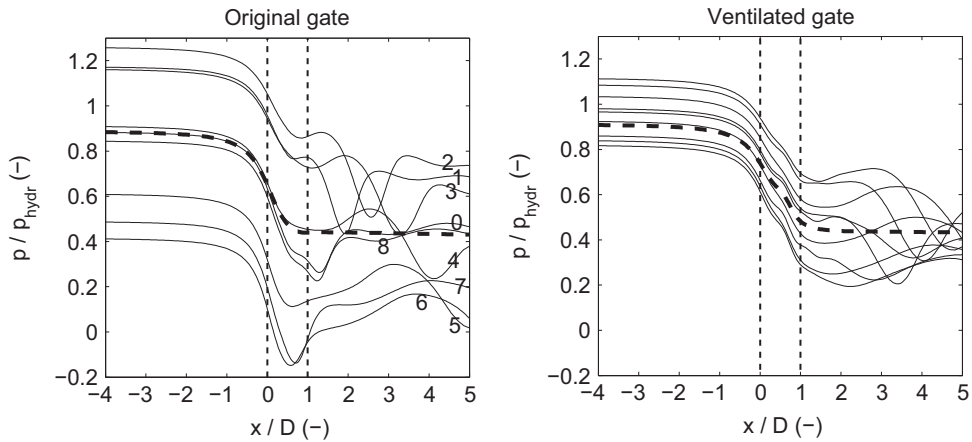


Fig. 11. Simulated streamwise pressure variation at  $z=a/2$  for moving gate without (left) and with ventilation holes (right);  $p_{hydr}$  is the hydrostatic pressure at  $z=a/2$ . Thick dashed lines show the situation where the gate is held fixed. Vertical thin dashed lines indicate location of the gate. The nine lines correspond to different moments in one full period, according to  $i\pi/4$  with  $0 \leq i \leq 8$ .

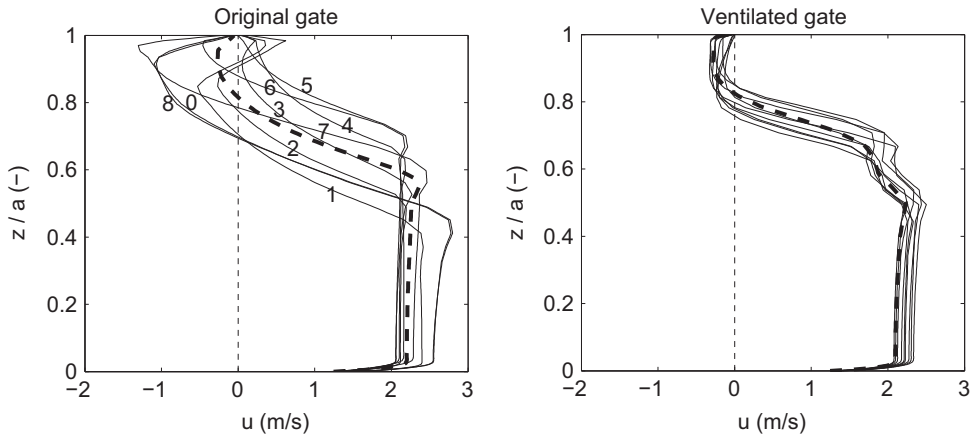
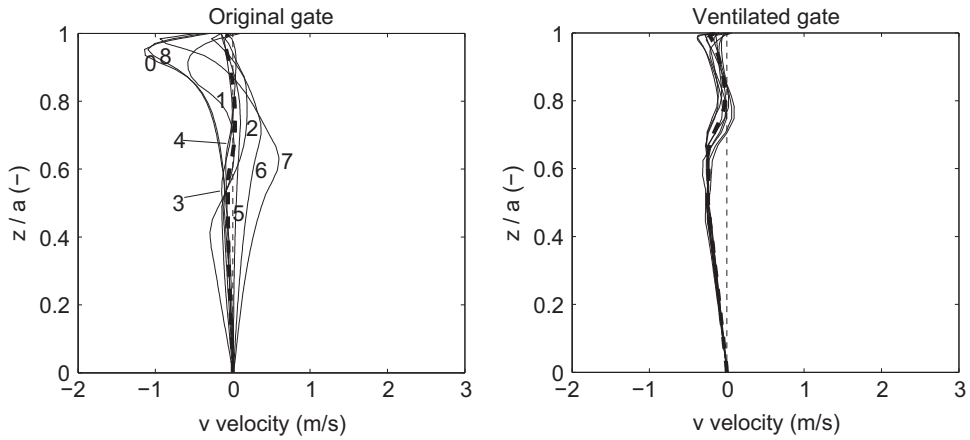
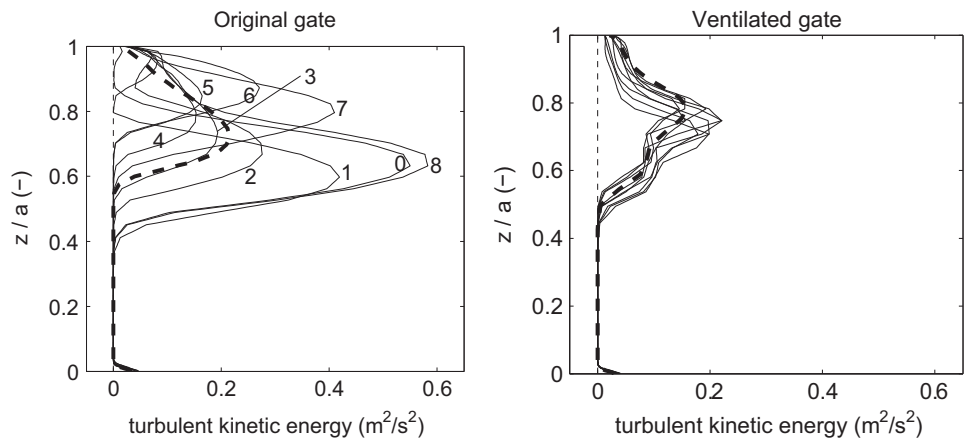


Fig. 12. Simulated vertical profile of horizontal velocity component  $u$  at downstream gate edge (from bottom to gate). Thick dashed lines indicate the fixed gate scenario. Positive values indicate the mean streamwise direction.



**Fig. 13.** Simulated vertical profile of vertical velocity component  $v$  at downstream gate edge (from bottom to gate). Thick dashed lines indicate fixed gate scenario. Positive values indicate upward direction.



**Fig. 14.** Turbulent kinetic energy in vertical profile at the trailing edge of the gate. Thick dashed lines indicate fixed gate scenario.

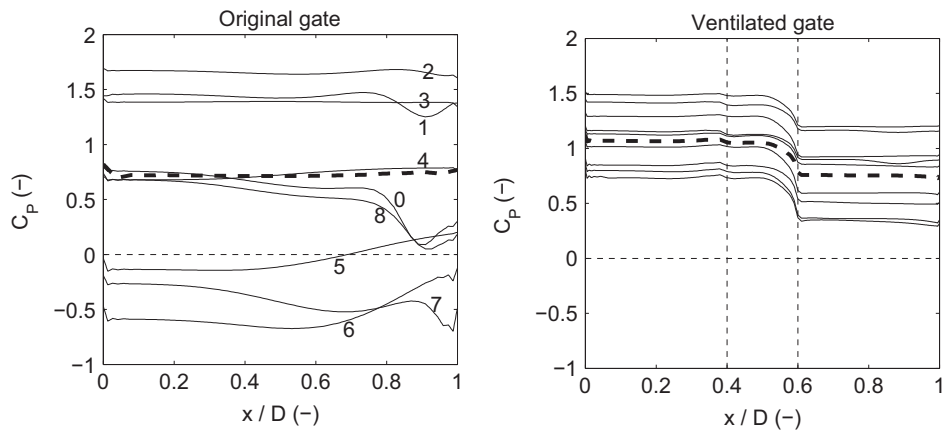


**Fig. 15.** Spatial variation of hydrodynamic pressure on the gate bottom boundary for both gate types. Thick dashed lines indicate fixed gate scenario. The vertical dashed lines show the location of the ventilation slot.

downstream edge of the slot outlet (upper part of profile) and from the leading edge of the gate bottom (lower part of profile).

The boundary pressures in Fig. 15 are given by the pressure parameter  $C_p$ , defined as the total pressure divided by  $\rho g \Delta h$ . The plots indicate that the reduced temporal fluctuation for the new gate results in positive pressures during the whole cycle, whereas the boundary pressure on the original gate is largely negative in the second part of the cycle when the gate is

between lowest and midway position. The spatial pressure variations towards the trailing edge of the original gate seem to signify unstable flow fluctuations. These are virtually absent at the slotted gate, for which a smooth pressure drop is visible across the outflow from the ventilation slot.

Fig. 16 gives more simulation results of both gate types for different moments in time for one oscillation period of case 2. Fig. C1 in Appendix C shows plots for case 1 for the original gate type.

The plots of pressure contour lines and flow velocity vectors in Fig. 16 serve to point out qualitative differences between the two gate types. Overall, the modified gate with ventilation slots has a flow field that is more constant in time with less vena contracta variation and less wake fluctuations. It can be seen that the flow through the slot works as an extra separated shear layer and also keeps instabilities from the wake away from the gate, see plots 3 and 4. At this time, during the first part of the upward movement, the reversion of streamwise flow velocity at the bottom boundary (which is part of a permanent recirculation zone) is strongest. Instantaneous spatial pressure gradients near the trailing edge appear for the gate without holes in plots 3 and 4. For the gate with slots this feature is not visible. This is discussed more deeply in Section 4.1 in the context of excitation. The jet through the hole persists in its downward flow during the whole oscillation period. This causes a relief in pressure build-up and prevents pressure fluctuations from the wake to enter the region under the gate. The intersections of contour pressure lines with the gate bottom present in the plots of the original gate help to illustrate the difference in pressure variations between the two gate types.

Comparing Fig. 16 with the simulations of case 1 for the original gate in Fig. C1, it is immediately clear that case 1 has a considerably more stable flow field. The vena contracta, the large wake recirculation and the small recirculation zone under the gate hardly vary in time.

Additional transient simulations with the gate held fixed (Fig. 17) again show the stronger reversed flow along the gate bottom for the gate without slots. There is also evidence for flow entering the near-bottom region from downstream, similar to plot 4 of Fig. 16. This entrainment feature is discussed in the next section. Table 3 gives the maximum flow velocities for the simulations. Velocities are much higher in the situation where the gate is free to move. There is little difference between the two gate types regarding maximum velocity. For the moving gate scenario the maxima were attained during the first part of the downward movement of the gate.

## 4. Discussion

### 4.1. Vibration mechanism

As explained in the introduction, past research largely agrees on the existence and working of two excitation mechanisms for cross-flow gate vibrations: ILEV and MIE (noise excitation or Extraneously Induced Excitation (EIE) is not considered here). Based on literature, the instability-induced or vortex-excited type is the most likely mechanism for the vibrations found around  $V_r \approx 2.5$ , while the movement-induced type is probably the dominant mechanism for the vibrations at  $V_r \approx 9.5$ .

Let us consider the fluid–structure dynamics of the original gate. The separation point is fixed at the sharp leading edge – irrespective of discharge and gate position – and the boundary pressure fluctuates near the trailing edge, both in space and time. However, given the fact that the strongest vibrations in the experiment occurred for conditions similar to case 1 (viz. at  $V_r \approx 2.5$ ), it is remarkable that the simulation of case 1 vibrations damped out. Runs with adapted settings in the neighborhood of case 1 (higher or lower gate opening, higher or lower discharge) were attempted, but did not yield different results. A transient simulation of case 1 conditions with the gate held fixed showed only small flow instabilities in the shear layer, making it impossible to determine the Strouhal number and identify small-scale vortices.

Simulation case 2 displays the main feature of movement-induced excitation (MIE) or self-excitation, because not only is a motion required to initiate the vibration process, the fluctuations in the boundary excitation force do not appear at all in the transient simulation when the gate position is fixed. The fact that the phase shift  $\varphi$  between excitation force and displacement is close to zero and the mean lift is only negative for a quarter of the period, implies that there is no direct evidence of galloping-type MIE excitation (Billeter and Staubli, 2000).

From the vector plots of the original gate (case 2), it is apparent that a delay exists between the motion of the gate and the oscillating shear layer. During the downward gate movement (plots 1–3 in Fig. 16), the reduction of the vena contracta lags behind the gate displacement, which results in a minimal vertical distance between the region of separated high velocity flow and the trailing edge at  $t=2.125$  s, at the lowest gate position. The profile plot of  $v$ -velocity in Fig. 13 shows that there is mild upward flow at  $x=D$  at this part of the period (from  $6\pi/4$  to  $7\pi/4$  or  $i=6, 7$ ), but it occurs away from the gate, with strongest  $v$ -velocities at  $z=0.5a-0.7a$ . As the gate moves upwards through the equilibrium position (plot 4 of Fig. 16, at  $t=2.175$  s), the vena contracta attains its minimum. This leaves a sizeable gap between separated flow and gate bottom. Clearly visible from the same plot, entrainment from the wake into the recirculation zone directly under the gate leads to high local velocities around the trailing edge. For a short time there is a small region of relatively low pressure at the trailing edge and the reverse flow coming from the wake seems to separate from the trailing edge as it moves from right to left in Fig. 16, plot 4. This phenomenon is reflected in the profile plots in Fig. 12 by negative  $u$ -velocities at  $0.8a < z < a$  for  $i=7, 8, 0, 1$ . The highest TKE levels are found at the same part of the period, see Fig. 14. The gate appears to receive a significant upward push from the pressure fluctuations associated with the entrainment. If this happens right at this moment of the period ( $t=2.175$  s, time step 4 in Fig. 16), as the results suggest, then this push does positive work on the gate

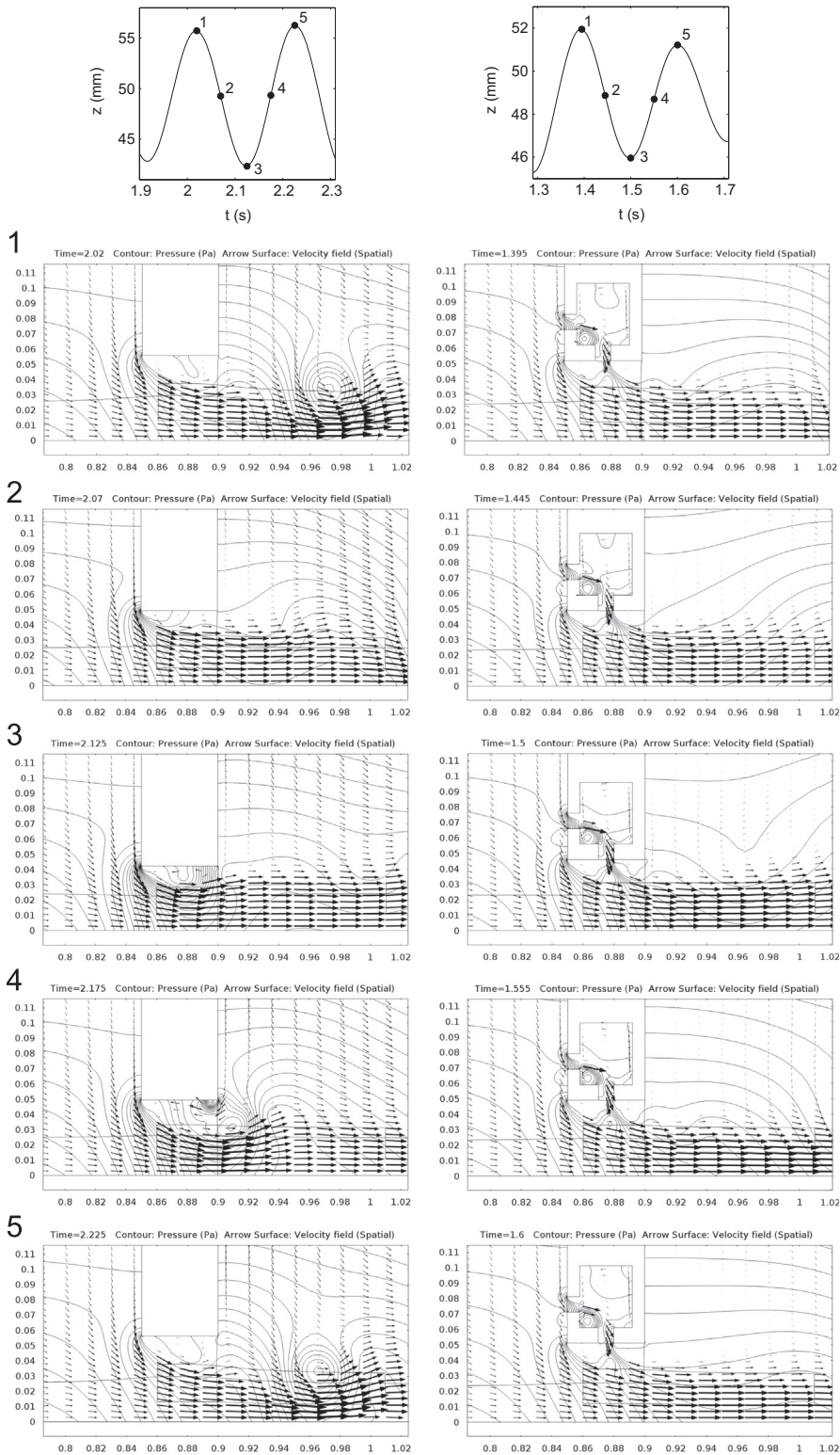


**Fig. 16.** Flow velocity vectors and pressure fields for the simulated motion of both gate types for case 2 ( $f=4.7$  Hz). The plots are numbered according to the time steps of one full period as indicated in the top plots. The original gate is shown on the left, the ventilated gate is shown on the right.

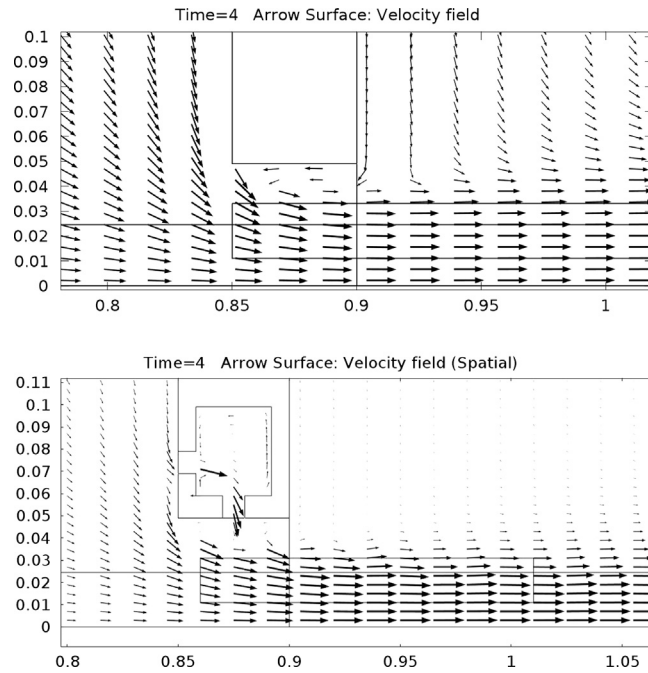


**Fig. 17.** Flow velocity vectors for the situation where the gate is fixed. Boundary conditions are according to case 2. The gate position corresponds to the equilibrium position of the moving gate simulations as given in Fig. 16.

**Table 3**  
Maximum simulated flow velocities for case 2.

	Moving gate (m/s)	Fixed gate
<b>Original gate</b>	3.38	2.38
<b>Ventilated gate</b>	3.30	2.40

motion, since it is in phase with the gate velocity. The vector plot suggests that this push takes place at  $x=0.6D-0.7D$ . However, the boundary pressure plot (Fig. 15) contains small dents for  $i=7, 8, 0, 1$  around  $x=0.9D$ , indicating that it might happen closer to the trailing edge. The movies of the original gate in the [Supplementary on-line material](#) provide further visual support of this excitation process.

Kolkman and Vrijer (1987) reported on a mechanism based on streamwise flow inertia caused by the discharge not instantly adapting to the new gate position during low frequency vibrations at small gate openings. Because the discharge is never choked in the numerical model, this mechanism is by definition not simulated. However, the role of this mechanism cannot easily be put aside, judging from the prominent streamwise pressure irregularities in the simulations.

#### 4.2. Effect of flow through the ventilated gate

Comparing the described entrainment effect of the original flat-bottom gate to the flow dynamics of the ventilated gate, as plotted in Fig. 16, it is seen that the vena contracta does not experience the same oscillatory variation. The free shear layer and the high velocity separated flow maintain a constant, safe distance from the gate bottom. Moreover, there are no signs of wake entrainment for the ventilated gate, so that an excitation by this mechanism must be absent. The profile plots in Figs. 11–15 demonstrate the lack of near-bottom pressure fluctuations capable of excitation by the virtual absence of negative  $u$ -velocities and positive  $v$ -velocities and much smaller TKE levels. The flow fields for the fixed gates (Fig. 17) illustrate the differences between the two gate types as well: the original gate shows reverse flow near the trailing edge and a significant recirculation bubble under the gate, while the two recirculation zones under the ventilated gate (that are visible only from close inspection) are smaller in size and have negligibly small velocities.

For the MIE mechanism, the general working of the leakage flow through the ventilated gate is that it alleviates the fluctuation of the streamwise pressure and the fluctuation of the boundary pressure (thus reducing or removing negative lift). In particular, it works by preventing wake fluctuations from entering the near-gate region. The simulations were unfortunately

unable to capture the effect of added slots in the case of vibration due to ILEV. It is plausible, however, that the leakage flow in this case disrupts the separated shear layer and vortices shed from the leading edge. The downward flow would consequently remove instabilities from the gate bottom and hence reduce the probability and impact of unstable reattachment.

The jet that flows out the middle of the bottom boundary not only removes local disturbances from the vicinity of the gate, as we have seen, but also has the effect of splitting the flat bottom surface into two parts as if there were two thin gates. This is favourable since thinner profiles are less prone to vibrations, or at least reduce the risky gate opening region. An alternative explanation of the response reduction could be found in the fact that the presence of the slot simply decreases the surface area for the lift pressure to work on. However, simulations of a closed rectangular gate with a bottom surface area equivalent to that of the gate with a hole showed that the diminished dynamic force amplitude cannot be explained by the smaller area. The different response must therefore be caused by the leakage flow.

The location of the outflow openings and the angle at which the jets flow (relative to the gate's bottom surface and the mean flow) are undoubtedly important design parameters. Another factor is the widthwise distribution of the slots in the design, that is, the distance between consecutive openings. A jet originating from flow through a small circular opening into a wide domain expands in all three dimensions, this is related to entrainment of surrounding fluid of relatively low velocities, an inherently turbulent process. The situation of flow through horizontal slots in the present study is different from the canonical jet, since the openings are elongated in one direction and the outflow domain has strong velocity gradients. The spaces between the slots, that were necessary in the present design to preserve structural rigidity, influence the outflows from the gate bottom slots and the three-dimensional aspect of the flow. So, although the slot configuration in this study is symmetric around the middle of the gate, three-dimensional flow phenomena may play a non-negligible role. The impact of this on gate stability and the effectiveness of the leakage flow can only be clarified through additional physical and numerical modelling.

#### 4.3. Implementation in prototype gates

In principle, there is no reason why the ventilated gate design would not be applicable to an actual gate. The gate would function as a conventional gate most of the time, with an added leak flow discharge through the ventilation slots. Perhaps the most critical issue is the gate's behaviour at very small gate openings, directly prior to full closure. In closed position, the leakage flow through the slots must be zero. This requires good seals that at the same time should not deteriorate the vibration properties of the gate's bottom geometry. The idea to add a movable element (gate or valve) to control the inflow through the upstream inflow slots seems interesting, but of course might engage itself in flow-induced vibrations. Another point of attention would be to prevent the accumulation of sediment and trash inside the ventilation holes.

#### 4.4. Evaluation of numerical modelling

The rigid-lid approach makes it impossible for the model to capture the effect of wave radiation. This is a form of hydraulic damping that involves vibration energy to be transformed irreversibly into free-surface waves. Not modelling this is not a severe omission, see also [Section 3.2](#). In the experiment wave radiation was only observed once at the upstream water surface in the low stiffness vibration region. Another free-surface effect that is completely neglected by using the rigid lid approximation is the coupling of flow-induced undulations of the downstream surface with the gate oscillation at increasing Froude number (see [Naudascher and Rockwell, 1994](#)). However, these undulations only occur at much lower submergence levels than investigated in this study. A consequence of the fixed free surface boundary in connection with the constant discharge is furthermore that global pressure oscillations are exaggerated. A lowering of the gate results in an immediate pressure increase in the upstream region, for instance. It is not easily found to what extent this affects the emergence of gate instabilities in the simulations; there is presumably a link with the representation of the MIE vibrations. The complication of this numerical modelling aspect lies in the fact that methods that do simulate the free surface (such as Volume Of Fluid or Phase Field) are usually not suitable for including both moving objects and turbulent flow, or they are computationally impractically expensive.

In physical experiments, comparisons of measured gate displacement and excitation force cannot always distinguish between added mass and rigidity since both coefficients are part of terms in-phase with the displacement (e.g. [Kolkman, 1984](#)). Similarly, in a numerical study it is not sufficiently clear whether a deviating response frequency should be attributed to artificial mass or rigidity effects. Either way, the distorting influence of artificial added coefficients must be elucidated before the full working of all physical mechanisms can be uncovered by numerical modelling.

Artificial damping or numerical diffusion can be traced back to the use of an implicit time scheme and 'consistent stabilisers' ([COMSOL, 2013](#)). The effect of this is inherent to the followed numerical approach; without it the simulation of the flow fails. Naturally, too much artificial damping of turbulent flow results in vibrations not being induced in the simulations where they do occur in real life. In particular, negative damping plays a key role in self-excited vibrations – if negative damping is neutralised by artificial factors, MIE-type vibrations will be inaccurately represented. As mentioned in [Section 4.1](#), another limitation of the numerical model is the constant discharge that in real life fluctuates as a result of gate displacements (most prominently for low frequency oscillations at small gate openings).

Finally, the obvious limitation of the RANS approach with a turbulence model is that not all turbulence scales are simulated. The fact that vortex shedding and velocity and pressure fluctuations at small-length scales connected to the shear

layer are parametrised too coarsely could be the reason why the (presumably ILEV-dominated) vibrations of case 1 were not reproduced. Applying a different turbulence model is unlikely to improve this; Large Eddy Simulation (LES) could be the only way forward.

## 5. Conclusions and future work

The aim of this study was to experimentally and numerically test a new hydraulic gate design for reducing flow-induced cross-flow vibrations. The addition of ventilation slots to a rectangular flat-bottom gate allowed a controlled leakage flow through the bottom of the gate, which produced a less severe vibration response compared to an unaltered reference gate.

The experimental data set fully covers the transitions between conditions with and without significant flow-induced vibrations in the reduced velocity region  $2 < V_r < 3.5$ . Two distinct vibration regimes are recognised with maximum response force amplitudes at  $V_r=2.54$  and  $V_r=10.16$  for gate openings  $a/D=0.48$  and  $a/D=0.86$ , respectively. The results show that the gate with perforated bottom profile significantly reduces cross-flow vibrations in the region  $2 < V_r < 3.5$ . Although not exhaustively covered, the measurements give reason to believe that the same holds for the higher region at  $V_r > 8.5$ . It was found that damping appeared to be higher for high hydraulic heads, but this did not affect the comparison between the two gate types.

The obtained data set was used to evaluate and improve the performance of a numerical model. Time-dependent FEM simulations on a moving grid were performed to solve the RANS equations for the flow and the gate displacement of the mass-spring system. An initial model validation step for the added mass in still water showed reasonable estimates compared to the measurements and reproduced the wall proximity effect. Subsequently, as a form of calibration, the sensitivity of the response frequency in flowing water to variation of the mass factor was used to select an appropriate solid density and spring stiffness while keeping the natural frequency in air equal to experimental values. Then, two cases of strong vibrations were simulated from the low and high  $V_r$  regions. For the high  $V_r$  case with response frequency 4.7 Hz, vibrations with growing amplitude were reproduced for the rectangular gate while the modified gate with a hole showed decreasing amplitudes in the same conditions. This matches results from the physical experiment.

Even though the numerical model does not capture all features relevant for a complete representation of the excitation mechanisms, the results nevertheless give valuable information about the working of the new gate design. The downward jets through the slots remove flow instabilities from the bottom boundary and smoothens local pressure gradients. In particular, the simulations show that for the standard rectangular gate, entrainment from the wake into the zone directly under the gate leads to a transfer of momentum from the flow to the gate. This movement-induced excitation is absent in the gate with slots, because the leakage flow prevents this entrainment. The combined results of measurements and numerical computations lead to the conclusion that the application of leakage flow is a promising new way to reduce the effect of flow-induced cross-flow gate vibrations at small gate openings.

The quantification of the fluid–structure interaction of gates is a challenging task. The approach followed in this study in which a physical experiment is complemented with physics-based numerical modelling is considered to be suitable for gaining understanding of gate design performance and excitation mechanisms. Future research should examine the new gate design in a wider range of conditions, most notably  $V_r > 9.5$ . Optimisation of the reduction effect of the leakage flow should be achieved by testing various slot geometries. Possible three-dimensional aspects of the flow have to be taken into account in this. Moreover, practical issues should be identified and addressed before real-life application is possible. For numerical modelling it is recommended to develop techniques that are able to combine FSI with simulations of the free surface and detailed turbulent flow.

Finally, the introduction of informatics in the field of hydraulic engineering has led to the application of data-driven modelling (Solomatine and Ostfeld, 2008). Obviously, this approach does not provide a direct way of understanding the physical mechanisms, but it can be very powerful in control systems. Erdbrink et al. (2012) presented the concept of a data-driven system to monitor and prevent flow-induced gate vibrations based on data from sensors on the gates. A similar proposal was reported by Han et al. (2011), but did not include artificial intelligence. The signals of the experimental data-set of this study are suitable for training a data-driven model to recognise transition characteristics when the gate approaches a region of high amplitude vibrations.

## Acknowledgements

The experiment was carried out at Deltares as part of project 1202229-004. We thank Tom Jongeling for his guidance in designing the measurement set-up and the supporting personnel at Deltares. This work is supported by the Leading Scientist Program of the Russian Federation, Contract 11.G34.31.0019 and by the “5-100-2020” Programme of the Ministry of Education and Science of the Russian Federation, Grant 074-U01.

## Appendix A. Numerical model equations

### A.1. Fluid domain

Time-dependent Reynolds-Averaged Navier–Stokes (RANS) equations for incompressible flow with  $k$ – $\varepsilon$  turbulence model are used

$$\rho \frac{\partial \bar{\mathbf{u}}}{\partial t} + \rho \bar{\mathbf{u}} \cdot \nabla \bar{\mathbf{u}} + \nabla \cdot \overline{(\rho \mathbf{u}' \otimes \mathbf{u}')} = -\nabla \bar{p} + \nabla \cdot \mu (\nabla \bar{\mathbf{u}} + (\nabla \bar{\mathbf{u}})^T) + \mathbf{F}_g, \quad (12)$$

$$\nabla \cdot \bar{\mathbf{u}} = 0, \quad (13)$$

where  $\rho$  is density of water,  $\mu$  is the dynamic viscosity of water,  $p$  is the water pressure, bars indicate time-averaged values and primes indicate variational variables. Furthermore

$$\bar{\mathbf{u}} = \begin{pmatrix} \bar{u} \\ \bar{v} \end{pmatrix}, \quad (14)$$

are the flow velocities and

$$\mathbf{F}_g = \begin{pmatrix} 0 \\ -\rho g \end{pmatrix}, \quad (15)$$

is gravity (force per unit volume).

The  $k$ – $\varepsilon$  turbulence model provides closure by solving a coupled pair of PDE's for turbulent kinetic energy  $k$  and turbulent dissipation  $\varepsilon$  (see COMSOL, 2013).

#### A.1.1. Boundary conditions

At the inlet a block velocity

$$\mathbf{u} = \begin{pmatrix} U_0 \\ 0 \end{pmatrix}, \quad (16)$$

with  $U_0$  a chosen constant.

At the outlet a hydrostatic pressure profile is imposed

$$p(y) = (h_{\text{out}} - y)\rho g, \quad (17)$$

where  $h_{\text{out}}$  is the water depth at the outlet, equal to the height of the flow domain.

Bottom flow boundary

$$\mathbf{u} = 0, \quad (18)$$

no slip with a wall function describing the near-wall velocity profile.

Boundary at water surface

$$\mathbf{u} \cdot \mathbf{n} = 0, \quad (19)$$

free slip or 'rigid lid'.

#### A.1.2. Initial conditions

At  $t=0$ ,  $p=0$  for all

$$(x, y), \text{ and } \mathbf{u} = \begin{pmatrix} U_0 \cdot \text{step}(t) \\ 0 \end{pmatrix}, \quad (20)$$

with  $\text{step}(t)$  a smooth S-curve increasing from 0 to 1 for  $0 < t < 0.5$  s.

#### A.1.3. Wall function condition

The wall lift-off (dimensionless wall distance) is defined as

$$y^+ = \frac{\rho u_\tau y}{\mu},$$

with shear or friction velocity.

$$u_\tau = C_\mu^{1/4} \sqrt{k}. \quad (21)$$

The condition for full resolution is  $y^+ = 11.06$ , the distance at which the viscous sub-layer and the logarithmic layer meet (see e.g. COMSOL, 2013).

## A.2. Solid domain

Defining  $\mathbf{u}_s = (u_{s,x}; u_{s,y})$  as the displacement vector of the solid body and  $\boldsymbol{\sigma}_s$  as the stresses it experiences (a tensor), we have

$$\rho_s \frac{\partial^2 \mathbf{u}_s}{\partial t^2} - \nabla \cdot \boldsymbol{\sigma}_s = \mathbf{F}_v. \quad (22)$$

The applied external forces  $\mathbf{F}_v$  acting on the gate body are

$$\mathbf{F}_v = \mathbf{F}_g + \mathbf{F}_{\text{spring}} + \mathbf{F}_{\text{water}} + \mathbf{F}_{\text{suspension}} = \begin{pmatrix} 0 \\ -\rho_s \mathbf{g} \end{pmatrix} + \begin{pmatrix} 0 \\ -k_{\text{spring}} u_{s,y} - c_{\text{spring}} \dot{u}_{s,y} \end{pmatrix} + \mathbf{F}_{\text{water}} + \mathbf{F}_{\text{suspension}}, \quad (23)$$

where  $\mathbf{F}_{\text{water}}$  represents the dynamic load of the water flow on the submerged part of the solid, see below. The spring force depends on chosen constants for stiffness,  $k_{\text{spring}}$ , and damping,  $c_{\text{spring}}$ . The last force represents the steady suspension force in the structural element that connects the gate object with the bigger (fixed) structure.

The constitutive relation (stress–strain relation) can be written as  $\boldsymbol{\sigma}_s = \boldsymbol{\sigma}_0 + C: (\boldsymbol{\varepsilon} - \boldsymbol{\varepsilon}_0)$  with subindex 0 indicating initial values;  $C$  is the elasticity, a function of the material properties (Young's modulus and Poisson ratio). The strain tensor is given by

$$\boldsymbol{\varepsilon}_s = \frac{1}{2} (\nabla \mathbf{u}_s + \nabla \mathbf{u}_s^T),$$

which is equivalent to

$$\varepsilon_{xx} = \frac{\partial u}{\partial x}, \varepsilon_{yy} = \frac{\partial v}{\partial y} \text{ and } \varepsilon_{xy} = \varepsilon_{yx} = \frac{1}{2} \left( \frac{\partial u}{\partial y} + \frac{\partial v}{\partial x} \right). \quad (24)$$

### A.2.1. Boundary conditions

Displacement is fixed in horizontal direction

$$u_{s,x} = 0. \quad (25)$$

### A.2.2. Initial conditions

$$\text{At } t = 0, \mathbf{u}_s = 0 \text{ and } \frac{\partial \mathbf{u}_s}{\partial t} = 0. \quad (26)$$

## A.3. Fluid–solid interface

### A.3.1. Boundary condition

The load that the water flow forces exert on the boundaries of the solid body,  $\mathbf{F}_{\text{water}}$ , is defined as a force per unit area (in N/m<sup>2</sup>)

$$\mathbf{F}_{\text{water}} = \mathbf{T} \cdot \mathbf{n}, \quad (27)$$

where  $\mathbf{n}$  is the normal vector on the solid boundary and  $\mathbf{T}$  is the  $2 \times 2$  tensor containing all stresses of the flow. The normal stresses, on the diagonal of  $\mathbf{T}$ , represent the pressure. The remaining elements of  $\mathbf{T}$  represent the viscous shear stresses – each of these elements consist of a stress contribution from the turbulent viscosity ( $\mu_T$ ) and the laminar viscosity ( $\mu$ ).

### A.3.2. Initial conditions

At  $t=0$ ,  $\mathbf{F}_{\text{water}} = 0$ , and subsequently

$$\mathbf{F}_{\text{water}} = \mathbf{T} \cdot \mathbf{n} \cdot \text{step}(t), \quad (28)$$

with the same S-function increasing from 0 to 1 for  $0 < t \leq 0.5$  s.

## A.4. Moving mesh

The whole domain (i.e. fluid and solid together) is subject to free mesh deformation. The boundary conditions for the mesh displacement vector  $\mathbf{u}_m$  are

$$u_{m,x} = 0, \quad (29)$$

on the fluid surface boundaries

$$\mathbf{u}_m = 0, \quad (30)$$

on all remaining boundaries of the fluid domain

$$\mathbf{u}_m = \mathbf{u}_s, \quad (31)$$

on the solid boundaries.

For the inner area, the mesh deformation is smoothed using hyper elastic smoothing, which is similar in form to the description of neo-Hookean materials (see COMSOL, 2013). This approach seeks for a minimum of 'mesh deformation energy' expressed as

$$W = \int_{\Omega} \frac{\mu}{2}(I_1 - 3) + \frac{\kappa}{2}(J - 1)^2 dV, \quad (32)$$

where  $\mu$  and  $\kappa$  are the equivalent constants representing shear and bulk moduli, respectively. Furthermore,  $J$  and  $I_1$  are the invariants

$$J = \det(\nabla_{\mathbf{x}}\mathbf{x}) \text{ and } I_1 = J^{-2/3} \text{tr}((\nabla_{\mathbf{x}}\mathbf{x})^T \nabla_{\mathbf{x}}\mathbf{x}), \quad (33)$$

where  $\det(A)$  denotes the determinant of matrix  $A$  and  $\text{tr}(A)$  denotes the trace of matrix  $A$ .

**Appendix B. Numerical simulations: gate response in time**

See Fig. B1.

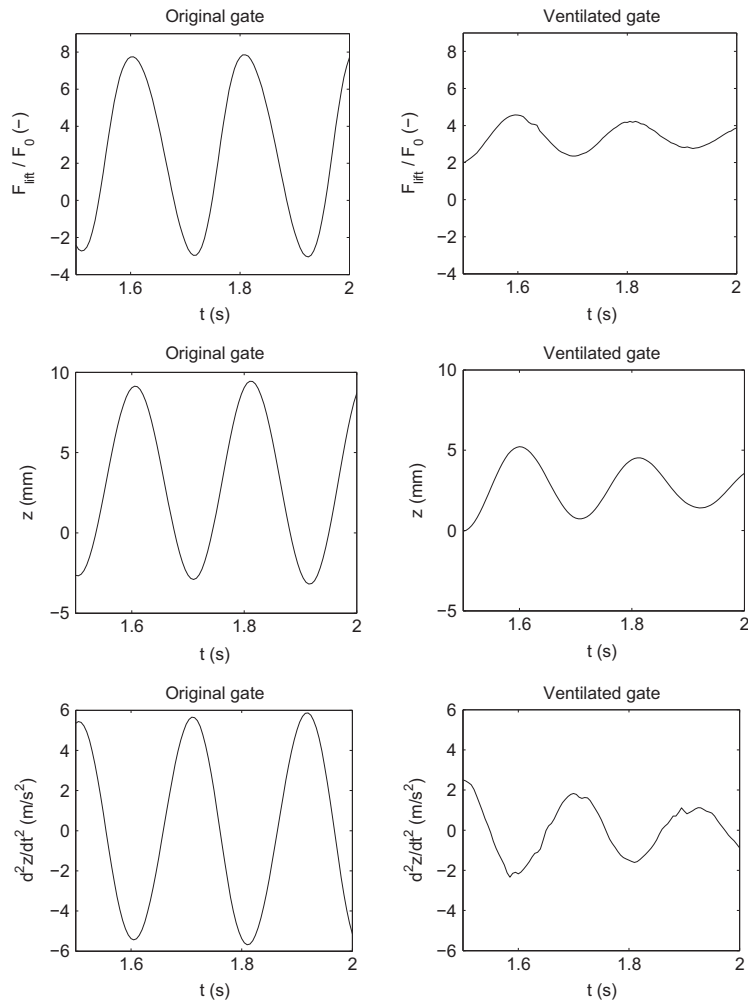


**Fig. B1.** Simulation case 2: time signal excerpts of dimensionless lift force, gate displacement and gate acceleration for both gate types. The acceleration is computed with a first-order finite-difference scheme without filtering.

Appendix C. Numerical simulations: flow velocity and pressure of case 1

See Fig. C1.

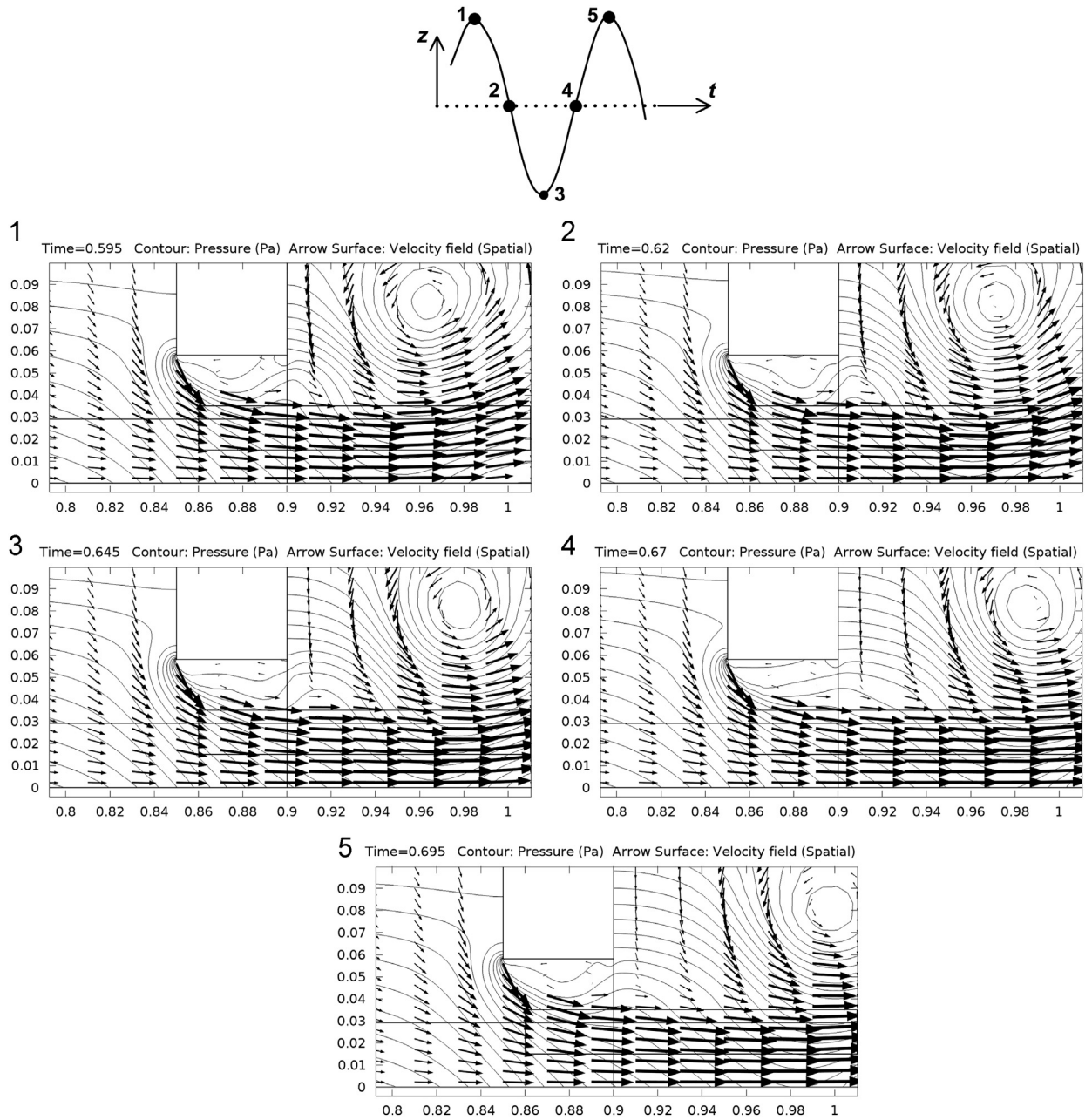


Fig. C1. Simulated flow fields for the original gate for case 1 of Table 2 ( $f = 10.1$  Hz).

## Appendix D. Supplementary materials

Supplementary data associated with this article can be found in the online version at <http://dx.doi.org/10.1016/j.jfluidstructs.2014.06.010>.

## References

- Al-Jamal, H., Dalton, C., 2004. Vortex induced vibrations using large eddy simulation at a moderate Reynolds number. *Journal of Fluids and Structures* 19, 73–92.
- Anami, K., Ishii, N., Knisely, C.W., 2012. Added mass and wave radiation damping for flow-induced rotational vibrations of skinplates of hydraulic gates. *Journal of Fluids and Structures* 35, 213–228.
- Billeter, P., Staubli, T., 2000. Flow-induced multiple-mode vibrations of gates with submerged discharge. *Journal of Fluids and Structures* 14, 323–338.
- Blevins, R.D., 1990. *Flow-induced Vibration*, second edition Van Nostrand Reinhold.
- COMSOL Multiphysics, 2013 Reference Guide v.4.3a and User Guide v4.3a. ([www.comsol.com](http://www.comsol.com)).
- Dai, H.L., Wang, L., Qian, Q., Ni, Q., 2013. Vortex-induced vibrations of pipes conveying fluid in the subcritical and supercritical regimes. *Journal of Fluids and Structures* 39, 322–334.
- De Boer, A., 2008. *Computational Fluid–Structure Interaction – Spatial Coupling, Coupling Shell and Mesh Deformation*. Ph.D. Thesis. Delft University of Technology.
- Den Hartog, J.P., 1956. *Mechanical Vibrations*. McGraw-Hill, New York.
- Erdbrink, C.D., 2012. *Physical Model Tests on Vertical Flow-induced Vibrations of an Underflow Gate – Part 3* (Deltares Report 1202229.004-HYE-005).
- Erdbrink, C.D., Krzhizhanovskaya, V.V., Sloot, P.M.A., 2012. Controlling flow-induced vibrations of flood barrier gates with data-driven and finite-element modelling. In: Klijn, F., Schweckendiek, T. (Eds.), *Comprehensive Flood Risk Management*. CRC Press/Balkema (Taylor & Francis group), Leiden. Proceedings of the 2nd European Conference on Flood Risk Management FLOODrisk2012, 20–22 November 2012, Rotterdam, The Netherlands, pp. 425–434. (<http://www.crcpress.com/product/isbn/9780415621441>).
- Erdbrink, C.D., Krzhizhanovskaya, V.V., Sloot, P.M.A., 2014. Free-surface flow simulations for discharge-based operation of hydraulic structure gates. *Journal of Hydroinformatics* 16 (1), 189–206. <http://dx.doi.org/10.2166/hydro.2013.215>.
- Ferziger, J.H., Perić, M., 2002. *Computational Methods for Fluid Dynamics*, 3rd edition Springer-Verlag, Berlin, Heidelberg, New York.
- Förster, C., Wall, W.A., Ramm, E., 2007. Artificial added mass instabilities in sequential staggered coupling of nonlinear structures and incompressible viscous flows. *Computational Methods Applied Mechanical Engineering* 196, 1278–1293.
- Gomes, J.P., Yigit, S., Lienhart, H., Schäfer, M., 2011. Experimental and numerical study on a laminar fluid–structure interaction reference test case. *Journal of Fluids and Structures* 27, 43–61.
- Han, P., Xue, H., He, Q., 2011. Monitoring technique and system of hydraulic vibration of sluice gate in long distance water conservancy project. *Procedia Engineering* 15, 933–937.
- Hardwick, J.D., 1974. Flow-induced vibration of vertical-lift gate. *ASCE Journal of Hydraulics Division* 100, 631–644.
- Ishii, N., 1992. Flow-induced vibrations of long-span gates. *Journal of Fluids and Structures* 6 (5), 539–562.
- Jaiman, R.K., Jiao, X., Geubelle, P.H., Loth, E., 2006. Conservative load transfer along curved fluid–solid interface with non-matching meshes. *Journal of Computational Physics* 218, 372–397.
- Jongeling, T.H.G., 1988. Flow-induced self-excited in-flow vibrations of gate plates. *Journal of Fluids and Structures* 2 (6), 541–566.
- Jongeling, T.H.G., Erdbrink, C.D., 2009. *Dynamica van beweegbare keringen* (“Dynamics of Movable Barriers”) (Deltares Report 1200216-000).
- Kanne, S., Naudascher, E., Wang, Y., 1991. On the mechanism of self-excited vertical vibration of underflow gates. Proceedings of the 5th International Conference on flow-induced vibration, Brighton, U.K., ImechE.
- Kapur, A.D., Reynolds, A.J., 1967. Reattachment downstream of a control gate. *Journal of Hydraulic Research* 5 (1), 1–14.
- Kolkman, P.A., 1976. *Flow-induced Gate Vibrations*. Ph.D. Thesis. Technische Hogeschool Delft (also Delft Hydraulics Laboratory Publication no. 164).
- Kolkman, P.A., 1980. Development of vibration-free gate design: learning from experience and theory. In: Naudascher, E., Rockwell, D. (Eds.), *Practical Experiences with Flow-induced Vibrations*; Proceedings of IAHR/IUTAM-symposium, Karlsruhe, 1979, Springer 1980. Also Delft Hydraulics Publication 219.
- Kolkman, P.A., 1984. Gate vibrations. In: Novak, P. (Ed.), *Developments in Hydraulic Engineering*, vol. 2, Elsevier Applied Science Publishers, London and New York. (chapter 2).
- Kolkman, P.A., 1988. A simple scheme for calculating the added mass of hydraulic gates. *Journal of Fluids and Structures* 2, 339–353.
- Kolkman, P.A., Vrijer, A., 1987. Vertical gate vibrations by galloping or by fluid inertia? Comments on the paper entitled “self-excited vibrations of vertical-lift gates” by N.D. Thang and E. Naudascher published in the IAHR *Journal of Hydraulic Research*, vol. 24, no. 5, 1986. *Journal of Hydraulic Research* 25 (3), 418–423.
- Liu, X., Zhao, L., Cao, H., Sun, X., 2011. Lifting force acting on a gate with high head. *Journal of Hydrodynamics* 23 (3), 379–383.
- Lupuleac, S., Bol'shev, A., Shinder, J., Petukhov, E., Chernetsov, V., 2008. The simulation of the Saint Petersburg flood defense system gate vibration under the loads from the moving water. In: Proceedings of 9th International Conference on Flow-Induced Vibrations FIV2008, Prague.
- Naudascher, E., 1991. *Hydrodynamic forces*, IAHR Hydraulic Design Manual Series, Taylor & Francis, Inc.
- Naudascher, E., Rockwell, D., 1980. Oscillator-model approach to the identification and assessment of flow-induced vibrations in a system. *IAHR Journal of Hydraulic Research* 18, 59–82.
- Naudascher, E., Rockwell, D., 1994. *Flow-induced Vibrations – An Engineering Guide*. Dover Publications, New York.
- Nguyen, D.T., 1982. Added mass behaviour and its characteristics at sluice gates. In: Proceedings of the International Conference on Flow Induced Vibrations in Fluid Engineering, Reading, UK, Paper A-2.
- Rugonyi, S., Bathe, K.J., 2001. On finite element analysis of fluid flows fully coupled with structural interactions. *Computer Modeling in Engineering and Sciences* 2 (2), 195–212.
- Sarpkaya, T., 2004. A critical review of the intrinsic nature of vortex-induced vibrations. *Journal of Fluids and Structures* 19, 389–447.
- Scheffermann, J.M., Stockstill, R.L., 2009. Pressures and discharges during operation of a lock valve – physical and numerical model results. *Journal of Hydraulic Research* 47 (1), 137–141.
- Solomatine, D.P., Ostfeld, A., 2008. Data-driven modelling: some past experiences and new approaches. *Journal of Hydroinformatics* 10 (1), 3–22.
- Thang, N.D., Naudascher, E., 1986a. Vortex-excited vibrations of underflow gates. *Journal of Hydraulic Research* 24 (2), 133–151.
- Thang, N.D., Naudascher, E., 1986b. Self-excited vibrations of vertical-lift gates. *Journal of Hydraulic Research* 24 (5), 391–404.
- Thang, N.D., 1990. Gate vibrations due to unstable flow separation. *Journal of Hydraulic Engineering* 116 (3), 342–361.
- Vrijer, A., 1979. Stability of vertically movable gates. In: Proceedings of the Symposium on Practical Experiences with flow-induced Vibrations, September 3–6, 1979, Karlsruhe. Also WL/Delft Hydraulics Publication no. 222.